



# BRNO UNIVERSITY OF TECHNOLOGY

VYSOKÉ UČENÍ TECHNICKÉ V BRNĚ

## FACULTY OF MECHANICAL ENGINEERING

FAKULTA STROJNÍHO INŽENÝRSTVÍ

## INSTITUTE OF PHYSICAL ENGINEERING

ÚSTAV FYZIKÁLNÍHO INŽENÝRSTVÍ

# SYSTEM FOR MAINTAINING THE SHARPNESS OF THE IMAGE FOR THE LIGHT MICROSCOPE

SYSTÉM PRO UDRŽOVÁNÍ OSTROSTI OBRAZU SVĚTELNÉHO MIKROSKOPU

## BACHELOR'S THESIS

BAKALÁŘSKÁ PRÁCE

## AUTHOR

AUTOR PRÁCE

Jakub Dokulil

## SUPERVISOR

VEDOUCÍ PRÁCE

Ing. Zbyněk Dostál, Ph.D.



## Zadání bakalářské práce

Ústav:	Ústav fyzikálního inženýrství
Student:	<b>Jakub Dokulil</b>
Studijní program:	Fyzikální inženýrství a nanotechnologie
Studijní obor:	bez specializace
Vedoucí práce:	<b>Ing. Zbyněk Dostál, Ph.D.</b>
Akademický rok:	2021/22

Ředitel ústavu Vám v souladu se zákonem č.111/1998 o vysokých školách a se Studijním a zkušebním řádem VUT v Brně určuje následující téma bakalářské práce:

### **Systém pro udržování ostrosti obrazu světelného mikroskopu**

#### **Stručná charakteristika problematiky úkolu:**

Pro světelnou mikroskopii živé buňky je nutné udržovat ostrý obraz vzorku během dlouhodobého pozorování. Z tohoto důvodu je nutné vytvořit vhodný opticko–mechanický systém, který toto zajistí.

#### **Cíle bakalářské práce:**

- 1) Provést rešerši vhodných optických metod.
- 2) Optimalizovat opticko–mechanickou stránku stávajícího systému.
- 3) Modul sjustovat.
- 4) Sestavit řídicí software.
- 5) Modul otestovat při dlouhodobém experimentu.

#### **Seznam doporučené literatury:**

FUKA, J. a HAVELKA, B. Optika a atomová fyzika: fyzikální kompendium pro vysoké školy. Praha: Státní pedagogické nakladatelství, 1961.

TÖRÖK, P a KAO, F. Optical imaging and microscopy: techniques and advanced systems. Springer, 2007.

GLÉZL, Š., KAMARÁD, J. a SLIMÁK, I. Přesná mechanika. Alfa, 1992.

Termín odevzdání bakalářské práce je stanoven časovým plánem akademického roku 2021/22

V Brně, dne

L. S.

---

prof. RNDr. Tomáš Šikola, CSc.  
ředitel ústavu

---

doc. Ing. Jaroslav Katolický, Ph.D.  
děkan fakulty



# Assignment Bachelor's Thesis

Institut: Institute of Physical Engineering  
Student: **Jakub Dokulil**  
Degree program: Physical Engineering and Nanotechnology  
Branch: no specialisation  
Supervisor: **Ing. Zbyněk Dostál, Ph.D.**  
Academic year: 2021/22

As provided for by the Act No. 111/98 Coll. on higher education institutions and the BUT Study and Examination Regulations, the director of the Institute hereby assigns the following topic of Bachelor's Thesis:

## **System for maintaining the sharpness of the image for the light microscope**

### **Recommended bibliography:**

FUKA, J. a HAVELKA, B. Optika a atomová fyzika: fyzikální kompendium pro vysoké školy. Praha: Státní pedagogické nakladatelství, 1961.

TÖRÖK, P a KAO, F. Optical imaging and microscopy: techniques and advanced systems. Springer, 2007.

GLÉZL, Š., KAMARÁD, J. a SLIMÁK, I. Přesná mechanika. Alfa, 1992.

Deadline for submission Bachelor's Thesis is given by the Schedule of the Academic year2021/22

In Brno,

L. S.

---

prof. RNDr. Tomáš Šikola, CSc.  
Director of the Institute

---

doc. Ing. Jaroslav Katolický, Ph.D.  
FME dean

## **Abstract**

Live imaging is a key tool for modern biological discoveries. However, without techniques for maintaining the sample in focus is hardly feasible. In this thesis I present an application of the optical vortices for the sample axial localization, so it will be maintained in focus. Experimental setup from previous experiments has been redesigned, so it could be integrated into the microscope. The setup has been built and successfully tested. To do this, the control software also had to be written. Also script with feedback loop for future integration into the microscope have been prepared.

## **Key words**

Vortex beams, axial localization, microscope, optical design.

## **Abstrakt**

Live imaging je klíčovým nástrojem pro moderní biologické objevy. Bez techniky pro udržení ostrosti obrazu je však stěží proveditelný. V této práci předkládám aplikaci optických vírů pro axiální lokalizaci vzorku tak, aby se obraz mikroskopu udržoval zaostřený. Experimentální sestava pro axiální lokalizaci z předchozích experimentů byla přepracována, aby se rapidně zmenšily její zástavbové rozměry, tak, aby jí bylo možné integrovat jako modul do mikroskopu. Sestava byla následně realizována a byla úspěšně experimentálně otestována. K tomu bylo třeba také navrhnout řídicí software. A připravit skript se zpětnou vazbou pro budoucí integraci do mikroskopu.

## **Klíčová slova**

Vírové svazky, axiální lokalizace, mikroskop, optický design.



## Declaration

I declare that this thesis has been composed by myself under the guidance of my supervisor and that it has not been submitted, in whole or in part, in any previous application for a degree. Any secondary sources and contributions from colleagues in the collaboration are explicitly referenced in the text.

Brno 20. of May 2022

DOKULIL, Jakub. *System for maintaining the sharpness of the image for the light microscope*. Brno, 2022. Available also at: <https://www.vutbr.cz/studenti/zav-prace/detail/140039>. Bachelor's Thesis. Brno University of Technology, Faculty of Mechanical Engineering, Institute of Physical Engineering. Supervisor Ing. Zbyněk Dostál, Ph.D.



*I would like to thank Zbyněk, my family and the people at the Institute of Physical Engineering for supporting me and giving me space.*



# Contents

<b>Introduction</b>	<b>1</b>
<b>1 Microscopy</b>	<b>3</b>
1.1 Optical microscope . . . . .	3
1.2 Microscopy methods for bioimaging . . . . .	4
1.3 Autofocus systems in microscopy . . . . .	11
<b>2 Thesis objectives</b>	<b>15</b>
<b>3 Optical vortices</b>	<b>17</b>
3.1 Mathematical description . . . . .	17
3.2 Axial localization . . . . .	19
<b>4 Experimental setup design</b>	<b>21</b>
4.1 Optical components . . . . .	21
4.2 Vortex mask design . . . . .	22
4.3 Vortex mask fabrication . . . . .	27
4.4 Optomechanics . . . . .	29
<b>5 Experiments</b>	<b>31</b>
5.1 Alignment . . . . .	31
5.2 Control software . . . . .	31
5.3 Image processing . . . . .	32
5.4 Experiments . . . . .	32
<b>Summary</b>	<b>37</b>



# Introduction

Microscopy is a key method for biological observations as the light microscope is able to observe intracellular processes. The live imaging technique enables to watch physiological processes in long time observations. This technique added a new dimension to the understanding of the cell function. However during the observation the specimen often shifts along the optical axes due the thermal expansion or biological processes. Therefore the system for maintaining the specimen in focus is needed.

For measuring the axial shift of the specimen seem the optical vortieces as a suitable method. Using properly chosen vortex beams the axial position of a point lightsource can be measured precisely.

---

# 1 Microscopy

## 1.1 Optical microscope

Microscope is a device used for observing small specimens and it has become one of the essential optical instruments. The scheme of the microscope may be seen in the figure 1.1. Initially, the microscopes consisted of the objective lens which images the specimen into the field plane. The specimen is then observed through eyepiece [1]. However today many manufacturers use another construction. The specimen is placed into the front focal plane of an objective and a collection of parallel beams is created. The beams are focused by the Tube lens into the field plane. The image is observed by the eyepiece. The objective and tube lens can be arbitrarily distant thanks to the characteristics of the collimated beams, there is an ‘infinite space’. Therefore this type of construction is called *infinite systems* [2].

The big manufacturers of microscopes, like Leica, Nikon, Olympus or Zeiss are using tube lenses different focal lengths  $f_{TL}$ . Objective lens with focal length  $f_{MO}$  combined with such a tube lens gives in plane field lateral magnification  $\beta$ ,

$$\beta = \frac{f_{TL}}{f_{MO}}. \quad (1.1)$$

It is the field plane image, that is recorded on the cameras.

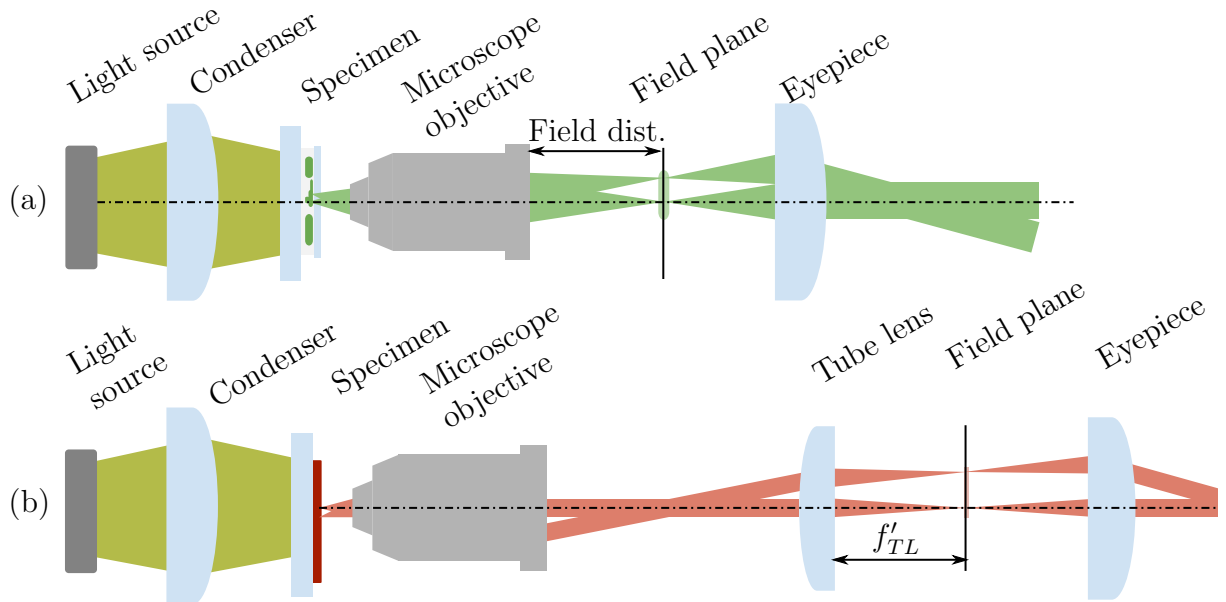


Figure 1.1: Scheme of an optical microscope. (a) The older microscope with finite tube length. (b) The infinite system. In the figure  $f_{TL}$  denotes tube lens focal length.

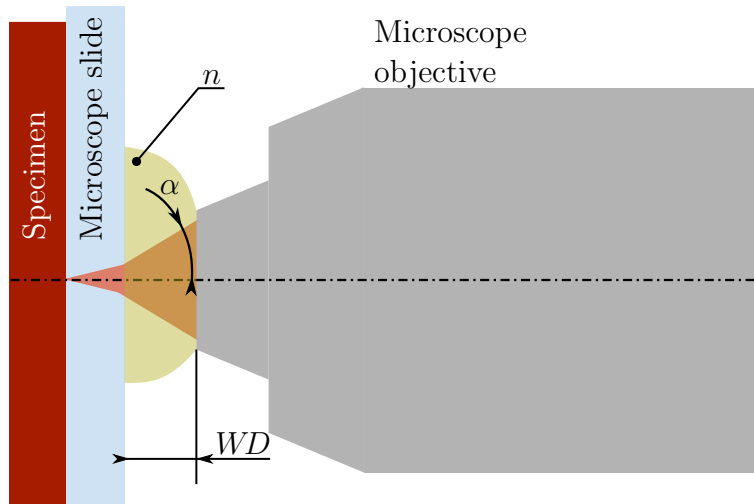


Figure 1.2: Parameters of an objective lens.

There are plenty of microscope objectives serving different purposes, since the objective lens is the most critical part of the microscope. The lens determines not only the magnification, however also the resolution, depth of focus, image aberration, light throughput and the field of view [3]. The manufacturers are using markings for objective types. *Plan* objectives have the field curvature correction. The chromatic aberration correction are called *Achromates* or *Apochromates* if they have chromatic aberration compensation for two respectively three wavelengths. The coverslip introduces a spherical aberration into the image. Therefore standardly are the lenses designed to compensate spherical aberration of 0.17 mm thick coverslip. However, some lenses have a ring to adjust this correction for different coverslip thicknesses. The different methods described later in section 1.2 may require special objective lenses, which are labeled so. For example DIC marks lens, which is suitable for differential interference contrast. Working Distance (WD) determines the distance between the first lens of the objective and the coverslip, see fig. 1.2.

The Numerical Aperture is a key characteristics of the lens. Let's denote the aperture angle  $\alpha$ , like in the fig. 1.2. With medium with index of refraction  $n$  is the *NA* of the objective

$$NA = n \sin \alpha. \quad (1.2)$$

The *NA* is crucial for the microscopes resolution as Ernst Abbe demonstrated [4]. With higher *NA* we are able to obtain better resolution. Unfortunately the total internal refraction on the microscope slide limits the aperture angle to about 40 degrees. Medium with higher index of refraction would increase not only the aperture angle, but also the whole *NA*. Therefore the so-called *immersive objectives* are used. As the medium is used water ( $n = 1.33$ ) or oil ( $n \sim 1.5$ ). The lenses have *NA* as high as 1.4, enabling them to obtain the resolution 240 nm [3].

## 1.2 Microscopy methods for bioimaging

One of the main application field of microscopy are life sciences. Optical microscopy is the main tool for cell and tissue observation with an impact to a wide range of biological disciplines. Even though the optical microscopy is also used in other fields, such as material research, further on will be written about microscopy in terms of biological applications.

The approach presented in the first paragraph is referred as *brightfield* and is the simplest microscopic technique. The image is formed thanks to light absorption by the specimen. However, there are other techniques in which the image is formed differently. These techniques enable to observe some samples, which may give a low contrast in brightfield observations and therefore be hardly observable.

Cells represent typical samples and are transparent. On the other hand, intracellular structures scatter light a little. With the scattered light being 10- to 20-fold lower in intensity [3] there may be low contrast in the image. The microscope technique called *darkfield* works with oblique lighting (see fig. 1.3), so the microscope objective collects only scattered light. This technique helps to enhance some intracellular structures.

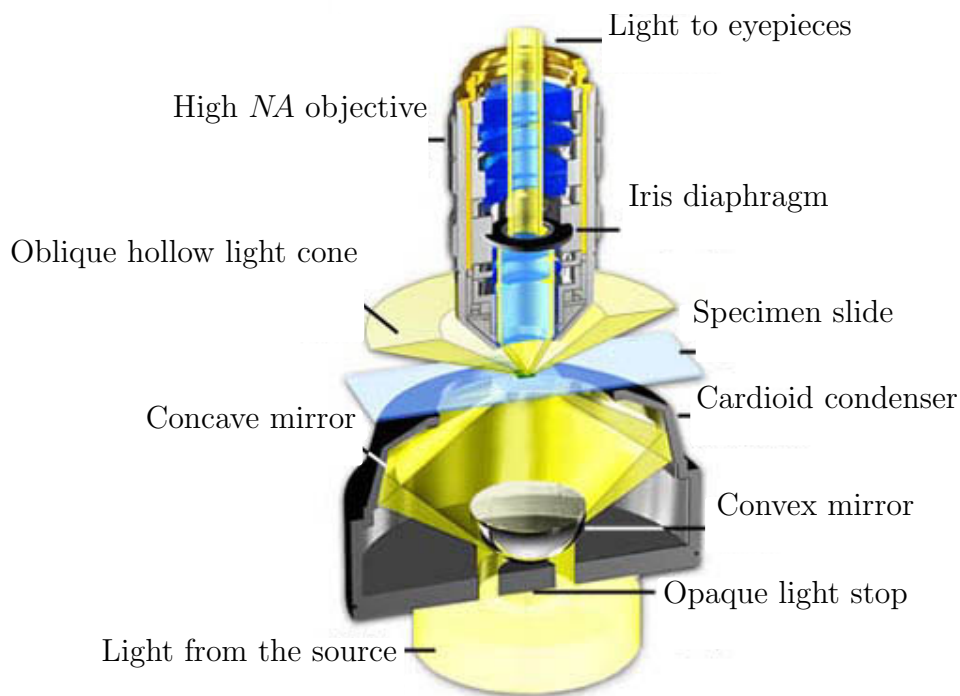


Figure 1.3: Scheme of an darkfield illumination. The oblique lighting means, that microscope objective collects only scattered light, which is further observed. Figure adapted from [5].

The cell organelles usually have a higher index of refraction compared to surrounding cytoplasm. Therefore the phase of rays scattered on the specimen is shifted around by  $\lambda/4$ . Dutch physicist Frits Zernike used this fact to build the *phase contrast microscope* and received a Nobel prize in physics [6, 7]. This microscope may be seen in the figure 1.4. The light passes through an annulus aperture and is then led up by a condenser into the specimen plane. The annulus aperture defines a section of the beam which is imaged into the specimen plane. The beam scatters on the specimen. As mentioned, the scattered light has a much lower intensity and shifted phase compared to the unscattered light. The light goes into the microscope objective with a phase plate in annulus shape inbuilt. The phase plate shifts the phase of unscattered light by  $\lambda/4$ , so it would interfere constructively with the scattered light. The phase plate also includes a gray filter ring which dims the intensity of unscattered light. The scattered and unscattered light interfere in the image plane.

Some specimens may have optically anisotropic behavior. This behaviour may be used

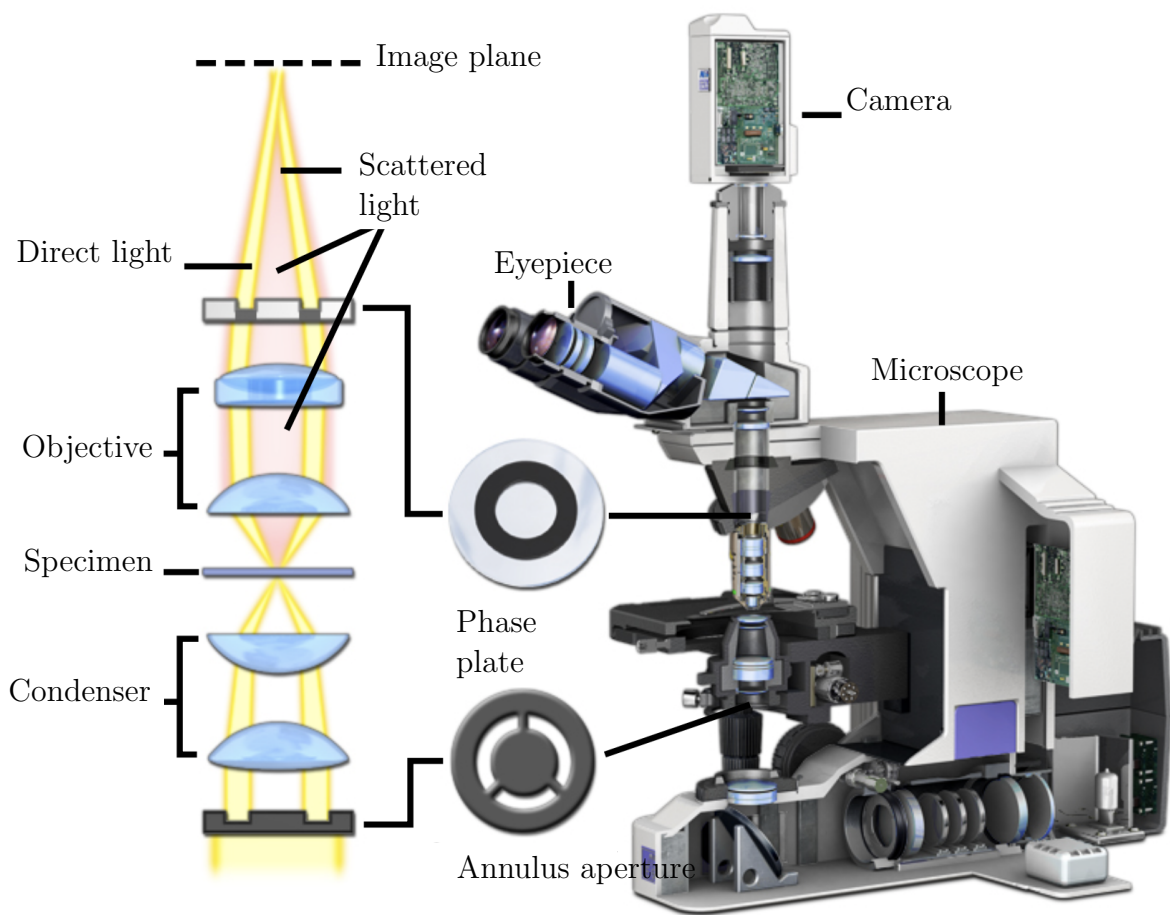


Figure 1.4: Phase contrast microscope. Figure adapted from [8].

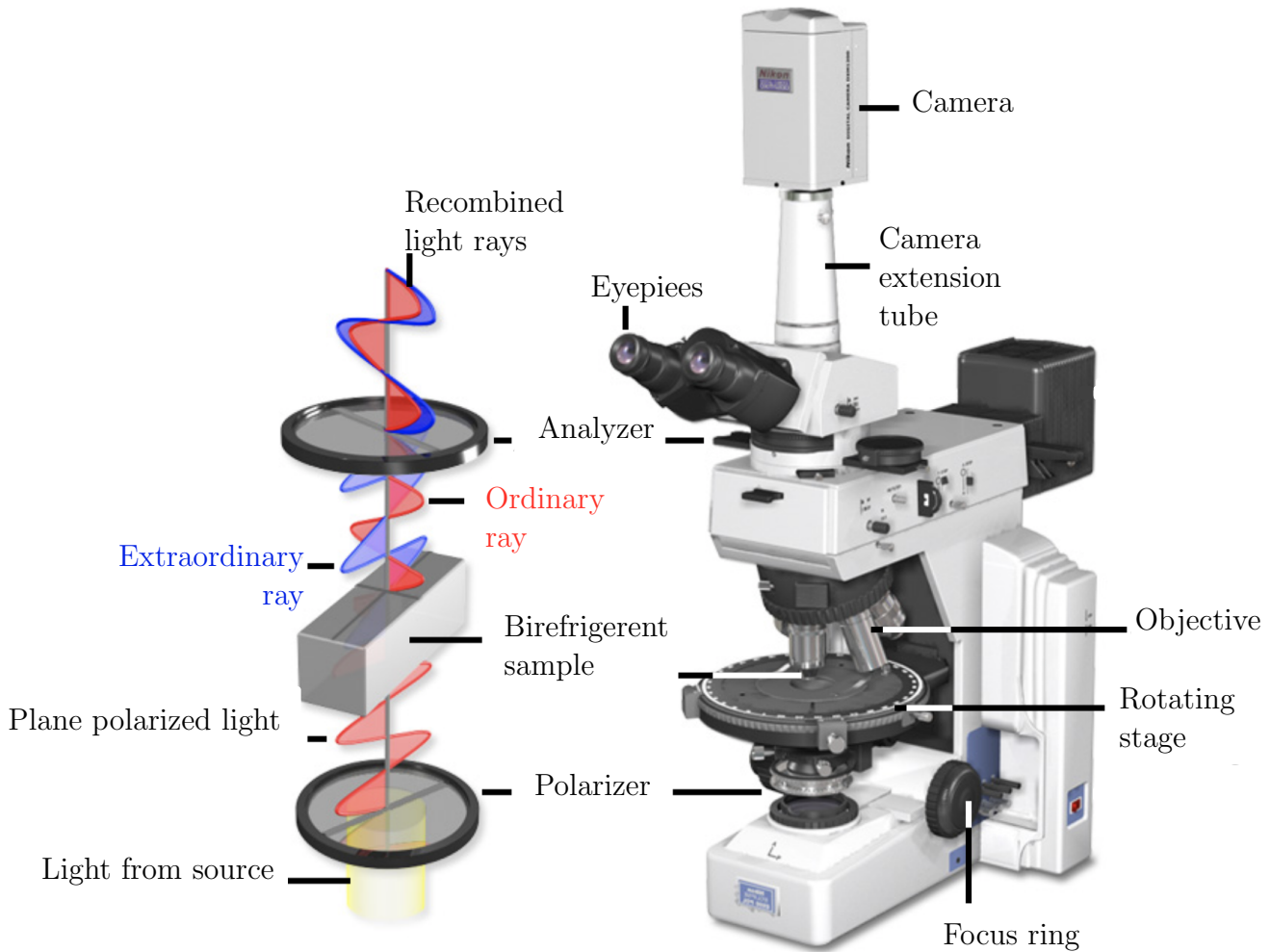


Figure 1.5: Scheme of a polarized light microscope. Figure adapted from [9].

in the *polarized light microscopy*. In this technique polarizer and analyzer are added to the setup, see fig 1.5. The light from the source is linearly polarized by the polarizer. The analyzer is placed between the objective and tube lens. The birefringent specimens produce two rays with mutually perpendicular polarisation – the ordinary and extraordinary rays. Those two rays propagate at different speeds and in general elliptical polarized light is created [3, 9]. Polarized light microscopy can enhance the contrast between isotropic and anisotropic areas in the specimen and finds its applications mainly in the technical sciences.

Nomarski went further with using the phase and polarisation properties of the intracellular organelles [3, 10]. *Differential Interference Contrast* (DIC) uses polarisation, however works also with specimen having no birefringent behaviour. For the scheme of such a microscope see figure 1.6. The polarized light is split by the Wollaston prism into two orthogonally polarized beams. The condenser shapes the beam. The rays are going through the specimen are shifted in phase. They are recombined with another Wollaston prism. The phase shift of two polarisations means the rotation of the polarisation vector. The rotation is proportional to the phase shift. Finally the light passes through the analyzer, which selects certain polarisation and therefore creates contrast.

The mentioned techniques, phase contrast, polarized light microscopy and DIC, use the different optical thicknesses of the observed organelles or their polarisation properties. Another way to get the contrast is to stain the cells, which is often combined with fluorescence

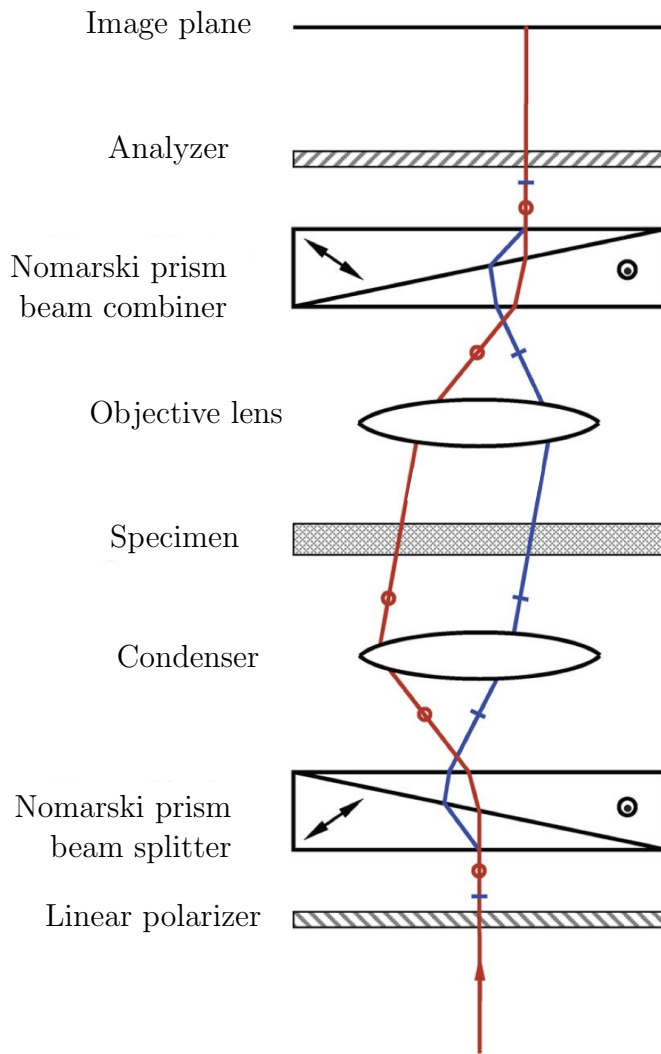


Figure 1.6: Scheme of a differential interference contrast microscope. Figure adapted from [11].

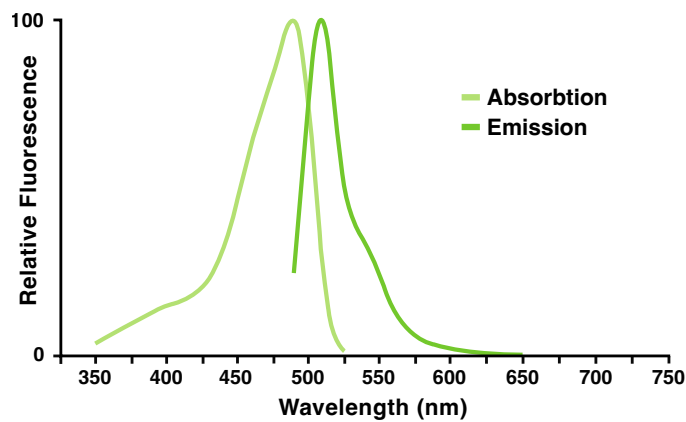


Figure 1.7: Absorption and emission spectra of the enhanced GFP (EGFP), one of the original GFP modifications. Adopted from [12].

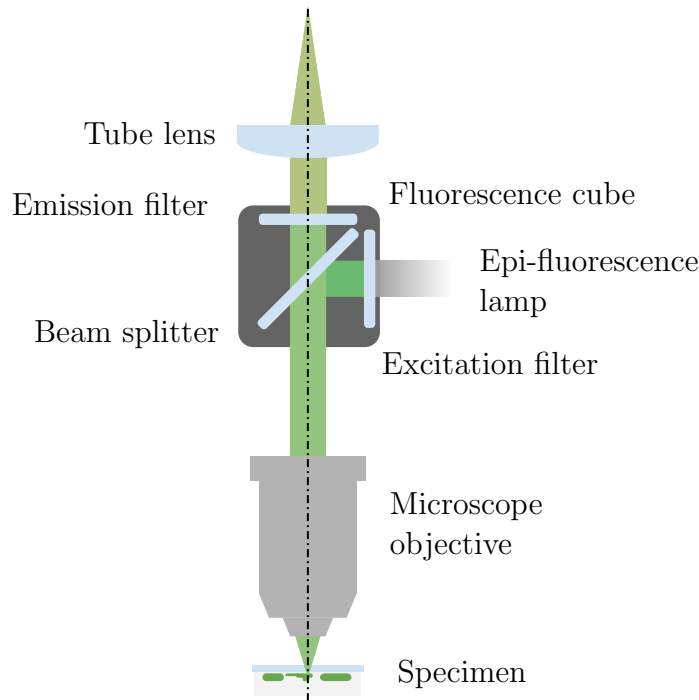


Figure 1.8: Scheme of a fluorescence microscope with detail of fluorescence cube.

imaging. With fluorescence labeling, we may observe labeled proteins or other intracellular molecules, which absorb and emits a defined band of wavelengths [13, 14]. However, photobleaching and phototoxicity may be limited while using fluorescence microscopy [15].

Each staining has a unique absorption and emission spectrum. The electron of the fluorophore is excited by the illumination photon into a higher energy state and ‘falls’ back into a lower state while meeting a photon with a lower wavelength. The rest of the energy is transformed into vibrational states. This shift in wavelengths is called *Stoke’s shift* and allows to separate the emitting light from the exciting with a proper filter. An example of a fluorescence microscope setup is shown in fig. 1.8.

One of the most significant stains is the Green Fluorescence Protein (GFP). This protein was originally extracted from *Aequorea victoria* jellyfish. The emission and absorption spectra may be seen in the figure 1.7. GFP has been modified to get different colors and also improved properties, e.g. stability of brightness. Enhanced GFP (EGFP) is an example of such an improvement. The color modifications are named after the colors, they are emitting like yellow (YFP), cyan (CFP) or blue (BFP) [16].

Fluorescence microscopy could be done also with multiple stains, however, this technique may be problematic as the emission spectra may share part of their peak tails. The different stains may be used for the enhancement of different structures.

Application of Fluorescence made possible the improvement of spatial and temporal resolution [16]. Furthermore, other techniques like confocal microscopy or superresolution techniques are using fluorescence to acquire the image.

In *confocal microscope* – see fig. 1.9 – is the exciting beam focused by the microscope objective into the spot. Emitting light is collected with the microscope objective, and imaged into the pinhole with a photodetector. The microscope scans with the beam through the field to obtain the image. The big advantage is a narrow depth of focus, as the pinhole lets minimum from the out-of-focus light through. This property is key for obtaining clearer images as with conventional fluorescence. Similarly, as in the fluorescence microscope, optical

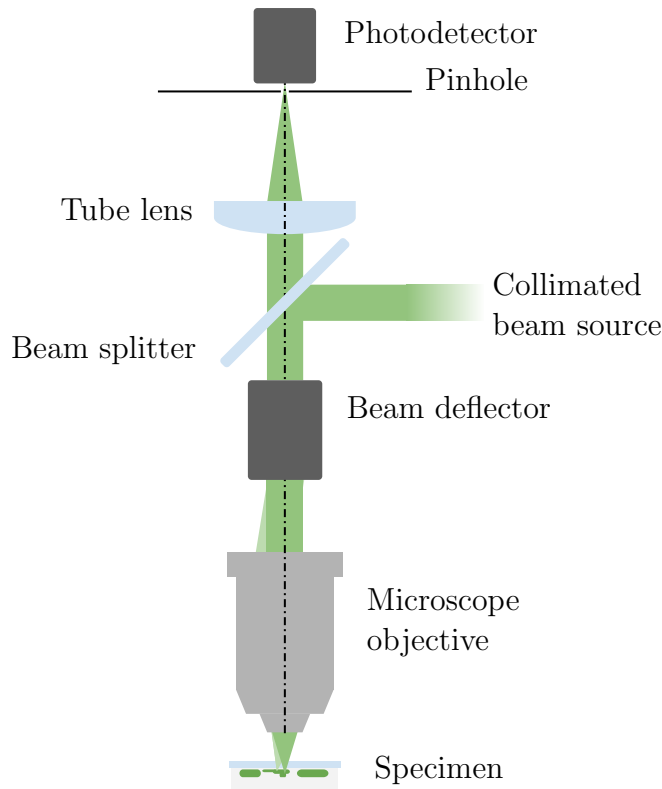


Figure 1.9: Scheme of a confocal microscope.

filters can be used, to cut off inappropriate wavelengths [3].

The fluorescence is also used in the super-resolution techniques which are capable to capture images with a resolution better than the diffraction limit. In 1994 Stefan Hell introduced the microscopy technique using the stimulated-emission-depletion (STED) [17]. Later on the Photoactivated Localization Microscopy (PALM) [18, 19] and stochastic optical reconstruction microscopy (STORM) [20]. The MINFLUX (minimal photon flux) microscopy enabled resolution in range units of nanometer [21]. The MINFLUX systems are sensitive to vibrations, so they are using adaptive feedback to maintain the system alligned during observations.

Earlier mentioned methods (phase contrast etc.) are using the optical properties of the sample to enhance the cotrast in the image. The Quantitative Phase Imaging (QPI) techniques go even further as they can get information about the optical thickness of the specimen. The techniques are mostly using two beams – specimen and reference beam. Interference of those two beams creates a hologram – image which contains information about both phase and intensity. The phase and intensity information is obtained by the reconstruction of the hologram. There are numerous implementations of QPI, the review from Park, Depeursinge and Propescu offer a good overview of this techniques [15].

Until now the imaging aspect of the technique has been described. However, the observation of living cells, referred to as *life imaging*, needs to consider other aspects, which are key for maintaining the cells alive. It is important to maintain the temperature, humidity or CO<sub>2</sub> concentration, so the cells stay alive during the long-term observation. For observation is key to keep the specimen in focus as the specimen may drift. This can be caused for example by temperature drift or air conditioning [22]. Also is important to avoid the cells from high exposures of light during the observation [23, 3]. Therefore autofocus (AF) systems are crucial for living cell observations.

In contrast to observations of fixed cells, with life imaging, we are able to observe cellular processes as they happen, for example how the cells react to some substance (e.g. drug). These observations added a new dimension to the understanding of cell function [22]. With life imaging, microscopy became a valuable technique in fields, where microscopy had not been used before [24]. Today live imaging plays a key role in cell biology, neurobiology, pharmacology, and developmental biology [23].

## 1.3 Autofocus systems in microscopy

Contemporary microscopes are often equipped with motorized stages which allows them to control the specimen position during the observation. One of the main purposes is to keep the specimen in focus during long-term observations. The specimen is maintained in focus by the stage movement. The input for the stage movement may result from the software image processing, which will be further referred to as a software AF, or the specimen position measurement – a hardware AF.

### Software AF

The software AF are using the *focus measure function* (FMF) to estimate how much is the image in focus. The FMF typically produces the bell-shaped curve as may be seen in the figure 1.10 [25]. Many of the FMFs were proposed in the 1970s-80s for the microscopy purposes [26, 27, 28, 29]. Comtemporarily known FMFs may be divided into the following categories [25, 30].

**Gradient based FMFs** assume, that the focused image contains more of the higher frequencies. The higher gradient means sharper edges in the image.

**Laplacian-based FMFs** also reflect the amount of sharp edges, however, use the second-order derivative.

**Wavelet-based FMF** calculate the frequency contents of the image using discrete wavelet transform coefficients.

**Statistics-based FMFs** use statistics to calculate the degree of focus.

There has been also a sucessfull implementation of Artificial Inteligence (AI) for improving the AF speed [31].

### Hardware AF

The hardware autofocus uses the optical pathway to measure the axial position of the sample. These systems are using Near Infra Red light (NIR) as the visible (VIS) light is used for observations. Hardware AF units are connected to the light pathway with a dichroic mirror.

One of the methods is the confocal pinhole detection (see figure 1.11). In this technique, a point light source is created in the specimen plane. The reflected light is passed through a confocal pinhole into the photodetector [32, 33].

In triangulation methods, half of the illumination beam is restricted by the half-moon aperture. The lateral position of the reflected light is then determined by the axial position of the sample. Such a system has been patented by Reinhamer [35]. Later on, the system

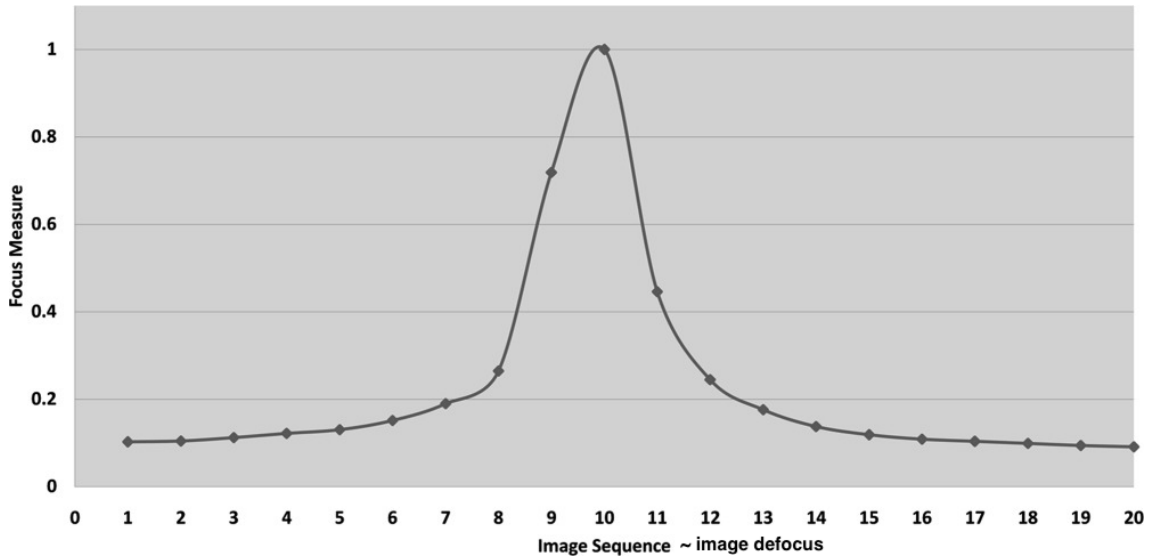


Figure 1.10: Bell-shaped curve typical for FMF. On the horizontal axes are numbers of pictures evaluated by the FMF proportional to defocus of the image. On the vertical axis is FMF in a.u. Adopted from [25].

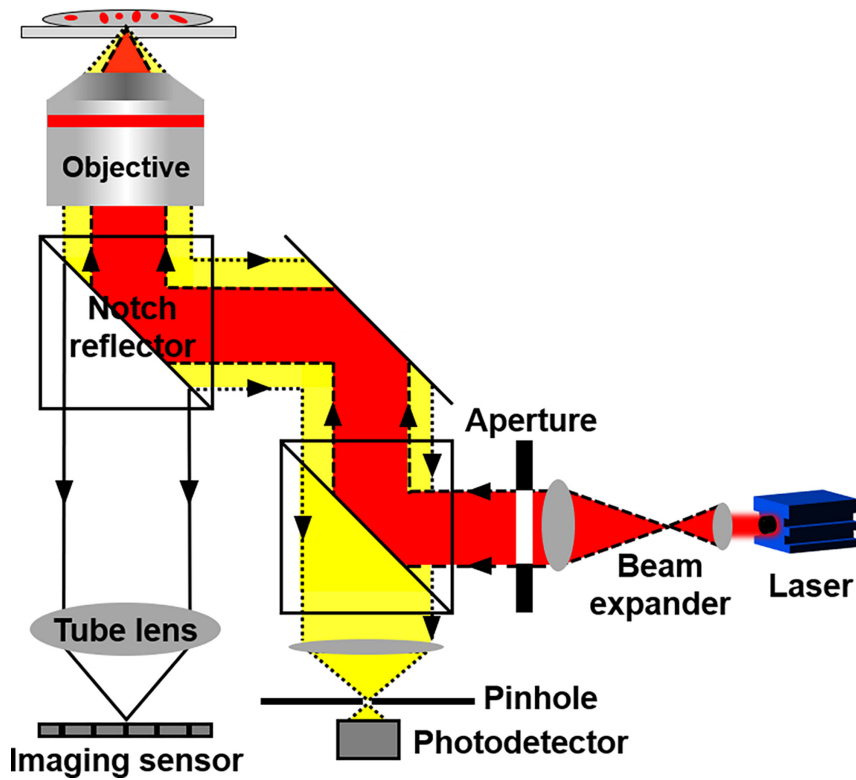


Figure 1.11: Pinhole detection AF system. Adopted from [32].

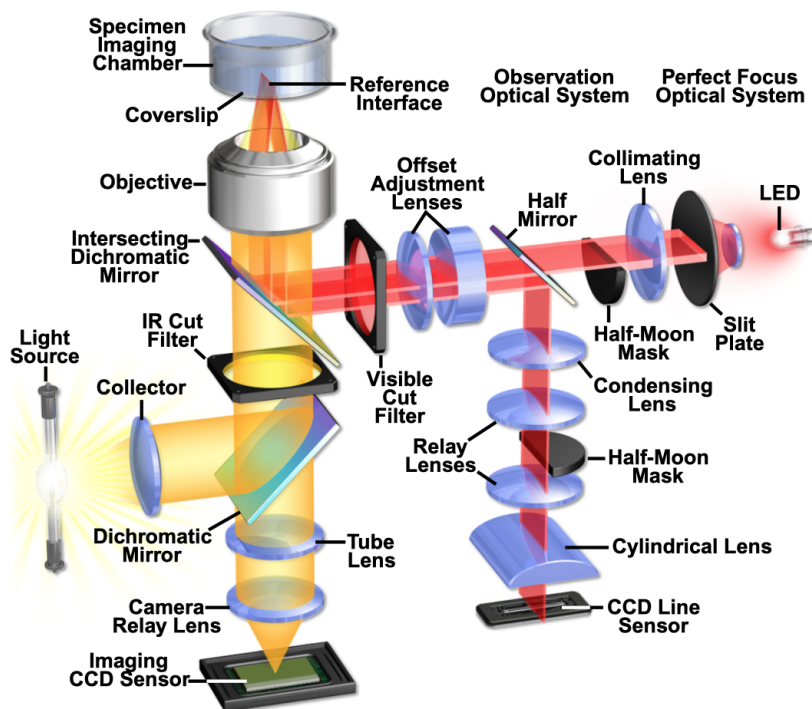


Figure 1.12: Nikon perfect focus optical scheme. Adopted from [34].

have been refined and implemented by Nikon as Perfect Focus System [32, 34] which may be seen in the figure 1.12.

Also, it is possible to use the beam splitter array like in the figure 1.13. Here the secondary focusing camera is used and the axial position is measured by the intensity of the signal in each sensor region. This technique have been patented by Virag *et al.* in 2008 [36].

Another approach is to use a tilted focusing sensor, on which is imaged an oblique cross-section of the sample. The optimum focus position is attributed to the contrast peak. This system may be seen in the figure 1.14 and have been implemented by Leica [37, 38].

Most digital single reflex cameras (DSLR) use so-called phase detection autofocus. The phase refers to the translational shift between two images. This technique has been also

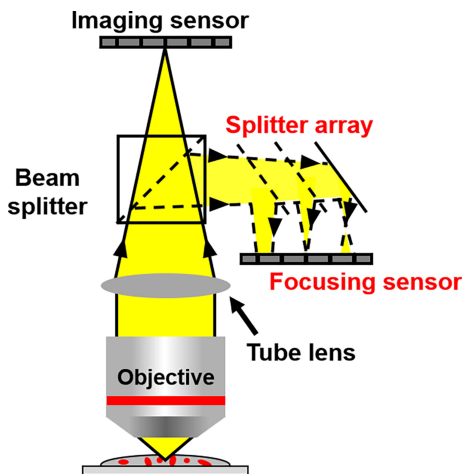


Figure 1.13: Beam splitter array autofocus. Adopted from [32].

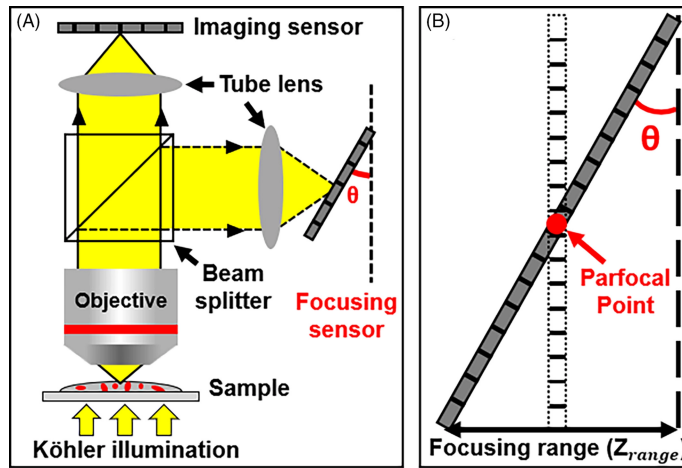


Figure 1.14: Tilted sensor autofocus. Adopted from [32].

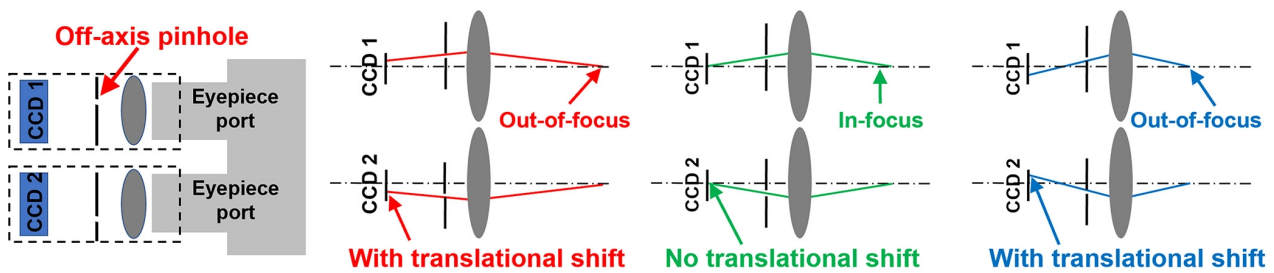


Figure 1.15: Phase detection autofocus. Adopted from [32].

adopted for microscopy [39]. The principle may be seen in the figure 1.15. Two pinhole modulated cameras are attached to the eyepiece for phase detection autofocus. If the sample is placed in focus, two cameras will capture identical images. If the sample moves out of focus, the images will be shifted. The shift is proportional to the defocus. The shift may be calculated via phase correlation in the frequency domain [32].

While using the software AF, the FMF is applied just on the part of the image (e.g. one cell), not to the whole image. Therefore if the cell changes the axial position the rest of the cells get out of focus. This happens for example during mythosis. Therefore is beneficial to use hardware AF, which holds the maintains the observation plane.

## 2 Thesis objectives

As was mentioned in the section 1.2, for live imaging is the hardware autofocus crucial. As the software solution is not always suitable. For example by meiosis observations, where the cells may distant from the coverslip. So if the software autofocus follows one cell, the others may occur out of focus. Therefore usage of the hardware autofocus brings better results during the long term observation. The axial localization using the rotating point spread function seems promising for creating a hardware autofocus module. To verify the suitability of this technique it is needed to:

1. Do a research on the axial localization using the rotating point spread function.
2. Optimize optical and mechanical properties of current system.
3. Align the module.
4. Write a driving software.
5. Test the module during long-time observation.



## 3 Optical vortieces

The first application of rotating PSF for axial localization was first shown in Greengard's paper [40]. Later on, was improved efficiency of energy transfer. In addition, have been shown that the use of a vortex mask could be used for purpose of axial localization [41]. This improvement led to many applications in microscopy [42, 43].

Presented technique based on the rotating PSF benefits from the precise axial localization. The usage of the NIR light in combination with a dichroic mirror does not disturb the observation. In addition, the NIR beam source with low intensity means the light is just a little phototoxic [44, 45, 46] and also selection of appropriate wavelength ( $\lambda < 1050$  nm) enables usage of the optical tweezers. Application of the spiral mask (SM) also means that no expensive adaptive device, such as Spatial Light Modulator (SLM) does not have to be used.

### 3.1 Mathematical description

The principle of the axial localization has been described for example in the paper [43]. Let's have a collimated monochromatic nondiffracting beam with complex amplitude  $U$ . As the system is cylindrical use of the cylindrical coordinates  $(r, \theta, z)$  will be beneficial. Therefore we unfold the wave vector  $\vec{k}$  ( $k$  denotes its magnitude) into the lateral and axial components, which we denote  $\alpha$  and  $\beta$ . Then we may write the complex amplitude of the beam as

$$U(r, \theta, z) = u(r, \theta; \alpha) e^{i\beta z} e^{i\kappa}, \quad (3.1)$$

where  $\kappa$  denotes the phase offset.

Now let the beam pass through the intermediate ring aperture. The aperture has infinite small thicknes and radius  $R$ . Using the Dirac  $\delta$  distribution the complex amplitude can be written as

$$U(r, \theta, z) = \delta(r - R) u(r, \theta; \alpha) e^{i\beta z} e^{i\kappa}. \quad (3.2)$$

In the next step let's shift, the phase of the beam proportinally to the beam by multiplying by  $e^{im\theta}$ , where  $m = \pm 1, \pm 2, \pm 3, \dots$ . The number of  $2\pi$  phase shifts per revolution  $m$  is an important property called *topological charge*. The schift can be obtained e.g. by special mask. This phase shift is illustrated in the figure 3.1. The beam amplitude is

$$U(r, \theta, z) = e^{im\theta} \delta(r - R) u(r, \theta; \alpha) e^{i\beta z} e^{i\kappa}. \quad (3.3)$$

Such a beam is called *vortex* and has a helical wavefront, which may be seen in the figure 3.1.

Now let's take such an amplitude as a Fourier spectrum and compose a beam from that by inverse Fourier transform. The ring radius  $R$  corresponds to the spatial frequency  $\alpha_R$ . The transform could be done by a lens with a focal length  $f$ . Then the frequency and radius are linked by the equation

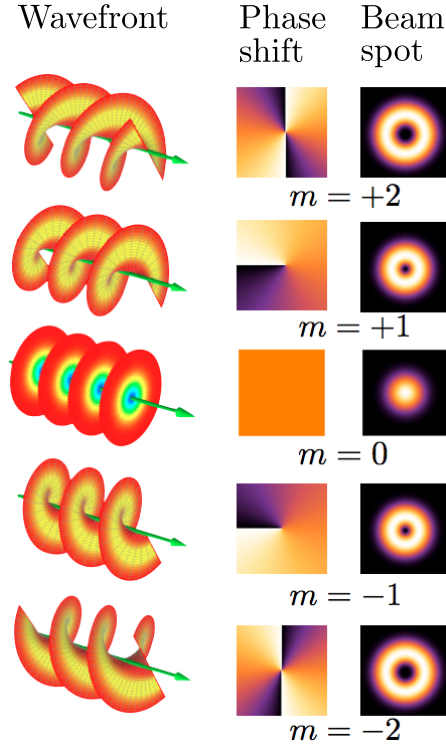


Figure 3.1: Illustration of vortex beams. Adopted from [47].

$$\alpha_R = k \frac{R}{f}.$$

Obtained beam has complex amplitude

$$U(r, \theta, z) = J_m(\alpha_R r) e^{im\theta} e^{i\beta z} e^{i\kappa}, \quad (3.4)$$

where  $J_m$  denotes the Bessel function of the first kind and  $m$ -th order. The intensity of created spot  $I$  is given by equation:

$$I = UU^* = J_m^2(\alpha_R r). \quad (3.5)$$

The spot intensity is independent on the  $\theta$  and  $z$  and has donut shape. Those donut shaped beams are for example used in superresolution techniques for creating deflection beams [17, 21].

Now combine two vortex beams created by spatial frequencies  $\alpha_1, \alpha_2$ , axial k-vectors components  $\beta_1, \beta_2$  and topological charges  $m_1, m_2$ . Letting those two beams interfere results in intensity [43]

$$\begin{aligned} I &= (U_1 + U_2) (U_1^* + U_2^*) \\ &= J_{|m_1|}^2(\alpha_1 r) + J_{|m_2|}^2(\alpha_2 r) + 2J_{|m_1|}(\alpha_1 r) J_{|m_2|}(\alpha_2 r) \cos(\Delta m \theta + \Delta \beta z + \Delta \kappa), \end{aligned} \quad (3.6)$$

where the last term is the interference term of the two beams, which is dependent on the topological charge difference  $\Delta m = m_2 - m_1$  and difference in the axial components of the  $\Delta \beta = \beta_2 - \beta_1$ .

Letting interfere generally  $N$  beams created by rings with normalized radiuses  $\rho_n$  and maximal radius  $R_{\max}$ . With each ring creating vortex beam with topological charge  $m_n$  the

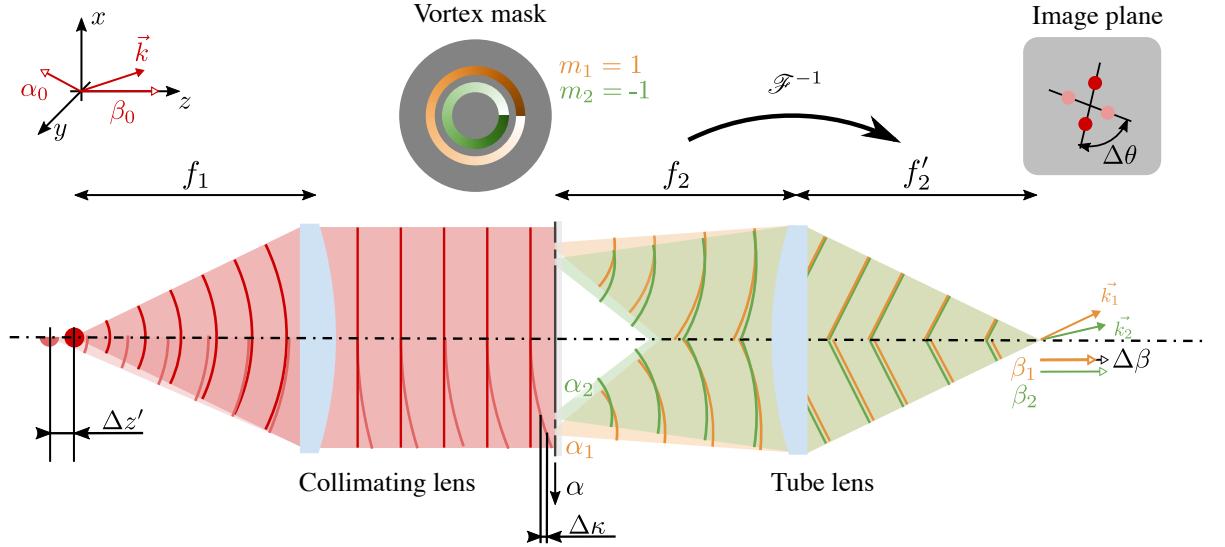


Figure 3.2: Simple setup for the axial localisation using the optical vortices. Colors ..

following conditions must be fulfilled for creating an PSF rotating with a defocus [43]

$$\rho_n = \sqrt{\frac{n}{N}}, \quad (3.7)$$

$$m_n = m_0 + n \Delta m. \quad (3.8)$$

## 3.2 Axial localization

Let us have a point light source. Putting the point into the focus of the lens we obtain a collimated beam like in the area above the axis in the figure 3.2 [48]. The beam passes through a mask with two zones creating vortex beams with topological charges  $m_1 = 1$  and  $m_2 = -1$ . The following tube lens with a focal length  $f_2$  creates inverse Fourier transform of the mask, which results into two bright blobs. The blobs we call Double Helix Point Spread Function (DH PSF).

Generally, two vortices with topological charge difference  $\Delta m$  can be used. The image then consists of  $\Delta m$  blobs.

The image intensity is described by the equation (3.6). The interference term determines how the image could be changed. The topological charge difference is given by the mask. However we may move the plane of the observation along the  $z$  axes, which causes the change of the term  $\Delta \beta z$ . Or the phase offset  $\Delta \kappa$  can be inserted between two beams. Such a situation is described in the lower half of the figure 3.2. The shift of the light point source by  $\Delta z$  creates a spherical wave incident to the mask. The spherical wave means the phase offset between the two vortex beams. The cosine in the interference term is linked with the azimuthal position  $\theta$ . Therefore change in the cosine argument results in the image rotation.

For small defocuses  $\Delta z'$  we can say the defocus is linearly proportional to the phase shift between two beams  $\Delta \kappa$ ,  $\Delta z' \sim \Delta \kappa$ . For describing the rotation of the image we need to find the angle which is added to the azimuthal angle  $\theta$  in the cosine argument. If the argument is constant

$$\Delta m \theta + \Delta \beta z + \Delta \kappa = \text{const.} \quad (3.9)$$

we obtain two relations describing the rotation

$$\theta \sim z, \quad (3.10)$$

$$\theta \sim \Delta\kappa. \quad (3.11)$$

Adding the assumption  $\Delta z' \sim \Delta\kappa$  we obtain

$$\theta \sim \Delta\kappa \sim z'. \quad (3.12)$$

In the original paper [43] was considered, that the mask will be placed in the plane optically conjugate with the rear focal plane of the collimator. Then the rotation in the image is linearly proportional to the image plane shift and defocus. We can define the period of rotation  $\Lambda$  as

$$\frac{d\theta}{dz'} = \frac{2\pi}{\Lambda}. \quad (3.13)$$

We obtain the period using the equation

$$\Lambda = \frac{4\pi N \Delta m f_1^2}{k R_{\max}^2}. \quad (3.14)$$

Taking into account the geometry of the beams the axial range  $L$  is

$$L = \frac{2\pi}{k} \frac{f_1^2}{\Delta R R_{\max}} \quad (3.15)$$

From the equation it is clear, that using a vortex mask it is possible to create a specially shaped DH PSF which rotates proportionally to the defocussation of the luminous point. This principle can be also used to the detection of the axial position of the specimen in the microscope to keep it in focus.

## 4 Experimental setup design

As has been shown in the theoretical part, the axial localization technique can be applied for measuring the specimen position, which can be used as an input for maintaining the specimen in focus. The setup from the figure 3.2 can be modified, so it can be added to the microscope. The module running on the IR wavelength should be connected with a microscope via dichroic mirror, so it would not disturb the observation. It is also needed to create a point source in the specimen plane. The image of a point source is then collimated and the light propagates to the mask. The mask is then imaged with a tube lens.

The selection of proper optical components is important for building a setup. Also, the mask needs to be designed and fabricated. Also, it is needed to choose proper optomechanical components, so the system could be aligned.

### 4.1 Optical components

The used setup may be seen in the figure 4.1. The light from the optical fiber is collimated and through the beam splitter and dichroic mirror reflected into the reflected into the microscope objective. The microscope objective creates an image of a point light source in the specimen plane. The defocussation of this point source will be measured. Together this part of the setup creates the *lighting part*. The light is reflected and passes to the vortex mask. The mask is placed in the front focal plane of the tube lens, so it would make an inverse Fourier transformation of the wave in the mask plane in the camera plane. The camera in the back focal plane observes the DH PSF. This part of the setup will be referred to as the *imaging part*.

The render of the realised setup may be seen in the figure 4.2 with the optical components listed in the table 4.1 [49, 50, 51].

The optical fiber is mounted in the beginning of the lightpath. The fiber coupled LED with peak wavelength 810 nm has been chosen, as it is a powerful light source bringing enough light to the system (LED has power up to 16 mW). It has a proper wavelength and it is an incoherent light source.

The beam from the fiber is narrowed by the beam expander and collimated. The combination of the beam expander and collimator has been chosen to create a beam with a spot as small as possible. The fiber with diameter 400  $\mu\text{m}$  must be narrowed. To do that, a beam expander must be added in the reverse direction. The beam expander virtually expands the distance between the fiber end and collimator and narrows the beam. The beam is then collimated with a collimator. The collimator has a focal length 200 mm and the expander has five times magnification. The beam is focused with a microscope objective into the coverslip plane.

The lighting part of the setup has been simulated in the Zemax ray-tracing program. As the components have unknown optical construction they were simulated as paraxial lenses. For the telescope focal lengths  $-20$  and  $100$  mm were chosen as they give the five times magnification. Through this system, an axial point and point  $200 \mu\text{m}$  laterally distant were

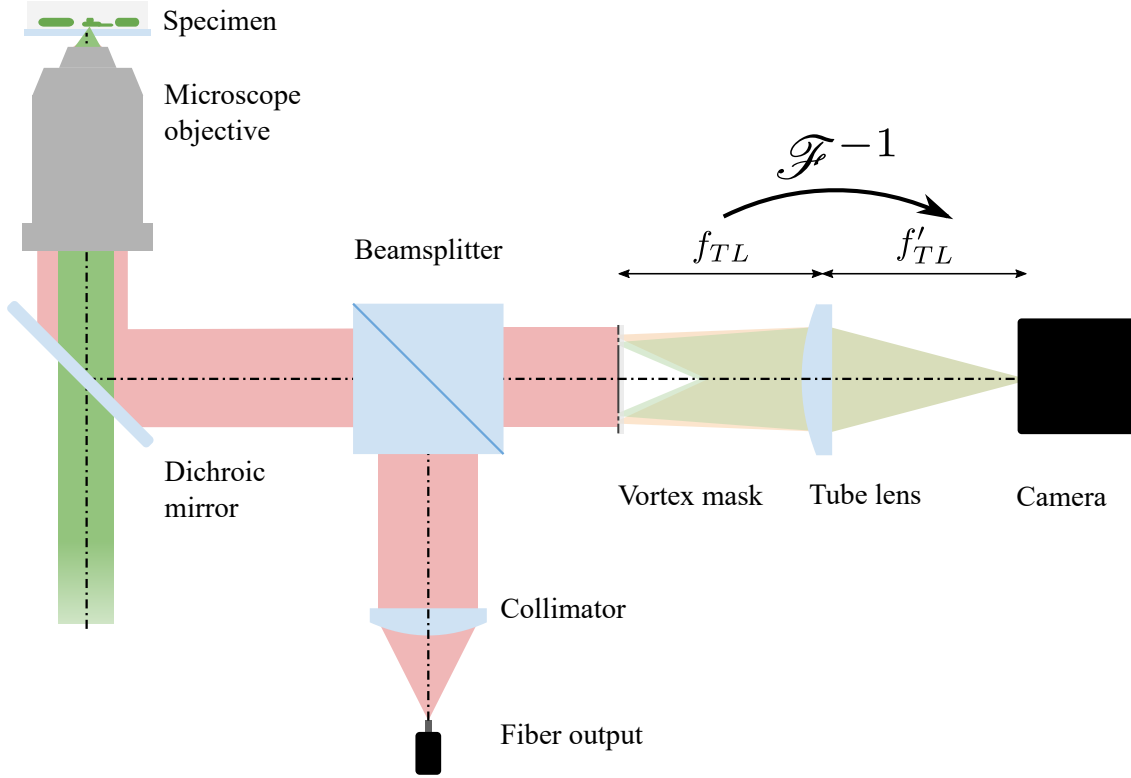


Figure 4.1: Scheme of the module.

imaged. See figure 4.6a for the layout. Based on this simulation the fiber is then imaged as a circle with diameter  $d_{10} = 0.67 \mu\text{m}$  while using Nikon Plan 10 microscope objective. Using Nikon Plan Fluor 20 objective the circle has diameter  $d_{20} = 0.344 \mu\text{m}$ . Both can be seen in the figure 4.6. According to Abbe resolution theory [4], two points distant  $d$  are resolvable if their distance is at least:

$$d = \frac{\lambda}{2NA}. \quad (4.1)$$

Where  $\lambda$  is the wavelength and  $NA$  is the microscope objectives numerical aperture. Using this equation the resolution limit is  $1.6 \mu\text{m}$  while using Nikon Plan 10 with  $NA = 0.25$ . For the Nikon Plan Fluor 20 ( $NA = 0.5$ ) is the limit  $0.81 \mu\text{m}$ . Those values are much bigger than the geometrical So the fiber is in both cases imaged into the diffractionally limited point.

The light is then reflected from the backside of the coverslip and returns through the beamsplitter to the vortex mask, which creates two vortices with topological charges  $m_1 = 1$ ,  $m_2 = -1$ . The inverse Fourier transform of the wave passing through the mask is then made by the tube lens. The plano-convex lens with focal length 125 mm has been chosen. The DH PSF is observed with the camera. The camera is equipped with Sony IMX477 sensor which benefits from the backside illuminated architecture [52]. The IR filter has also been removed from the camera to increase sensitivity.

## 4.2 Vortex mask design

In section 3.2 we assumed infinite thin rings in the Vortex mask. Such rigs are beneficial for the analytical computation of the DH PSF. However, in reality, they would not transmit any light. In practice, two types of masks are used [54]. The first type may be seen in the figure

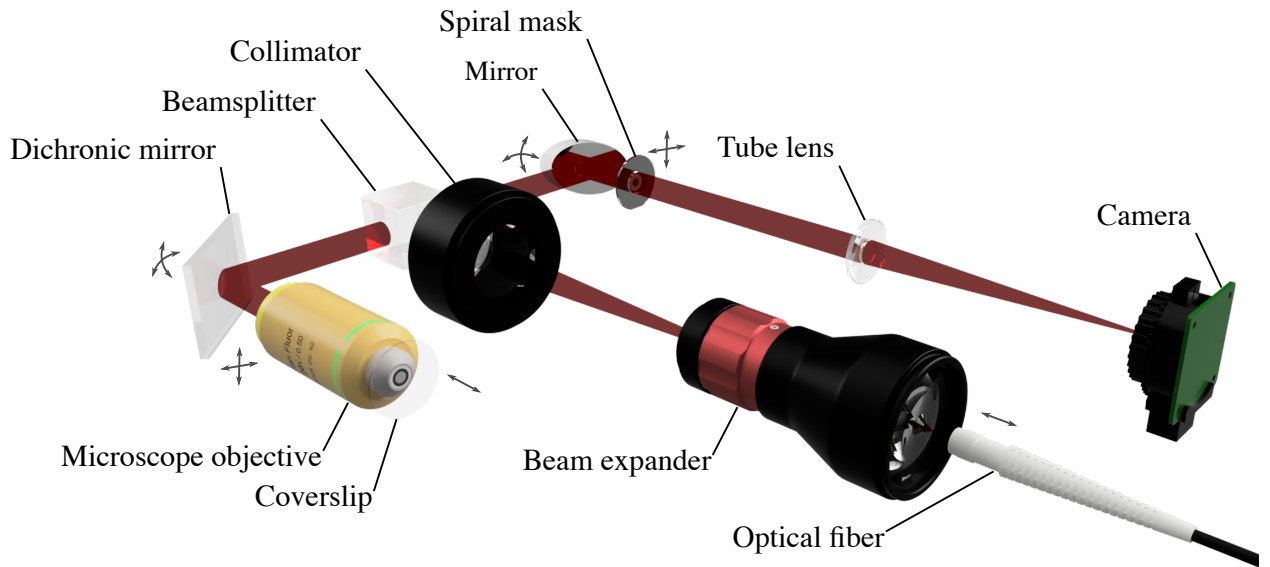


Figure 4.2: Render of the laboratory setup. The gray arrows illustrate fine optomechanical mounts for alignment.

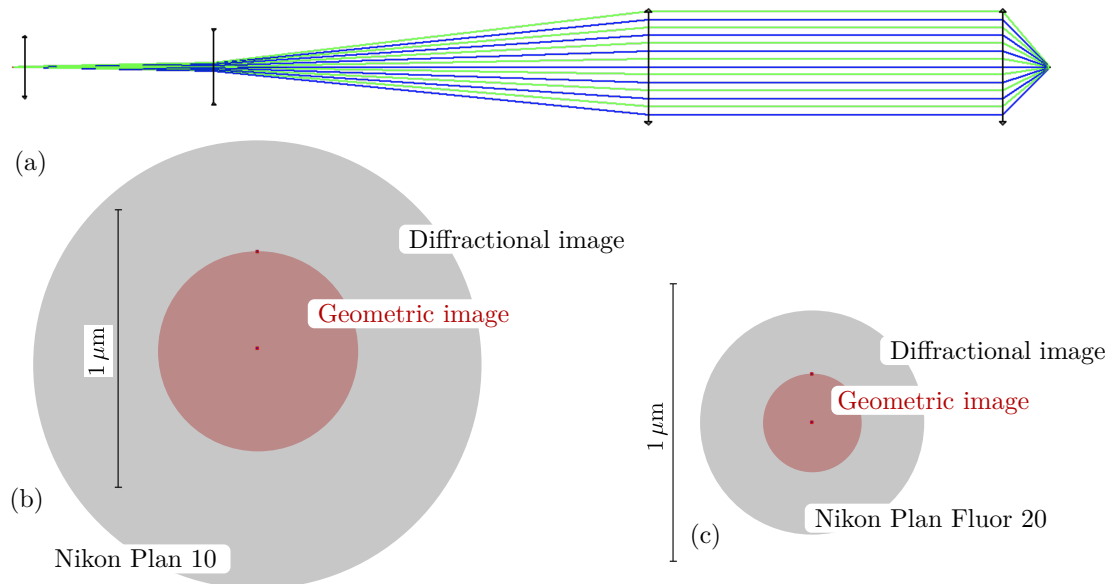


Figure 4.3: Simulation of the lighting part carried out in Zemax ray-tracing program. (a) Layout. (b) Spot diagram, using Nikon Plan 10 objective. (c) Spot diagram, using Nikon Plan Fluor 20 objective.

Table 4.1: List of used optical components [49, 50, 51].

Component	Part no.	Manufacturer
Fiber pigtailed LED	EP810S04 – 810 nm	Thorlabs Inc.
Beam expander 5×	GBE05-B	Thorlabs Inc.
Collimator $f = 200$ mm	TTL200-A	Thorlabs Inc.
Beamsplitter	CCM1-BS014	Thorlabs Inc.
Dichronic mirror	DMBP740B	Thorlabs Inc.
Mirror	PFE10G01	Thorlabs Inc.
Tube lens $f = 125$ mm	LA1986-B	Thorlabs Inc.
Camera	RaspberryPi High Quality Camera	Raspberry Pi
Microscope objective	Nikon Plan 10	Nikon Instruments Inc.
Microscope objective	Nikon Plan Fluor 20	Nikon Instruments Inc.

Table 4.2: List of used mechanical components [49, 53].

Component	Part no.	Manufacturer
Z-axis mount	SM1ZA	Thorlabs Inc.
XY mount	CXY1A	Thorlabs Inc.
Right-angle kinematic mirror mount	KCB1	Thorlabs Inc.
Linear piezo stage	SLC-2430	SmarAct GmbH.

4.4a. The mask has thin ring zones, which makes it resistant to phase changes, which may occur across each zone due to the aberrations. The second type has wide zones and may be found in the figure 4.4b. The mask with wide zones is not as aberration resistant as the one with thinner ones. However wider zones transmit more light, which may be beneficial in some light-sensitive applications.

For the experimental setup, I have decided to use the mask with thin ring zones. For the dimensions of the mask see the drawing in the figure 4.5. The size of the mask is determined by the size of the microscope objective aperture stop. The Nikon Plan Fluor 20 objective has aperture stop with diameter 11 mm. So with the reserve, I have decided the biggest diameter to be 7.5 mm.

For the purpose of the mask design verification, I have simulated the behaviour of the mask with a script written in Python language. The simulation follows the figure 4.6. The point source displaced by  $\Delta z'$  from the focal point of the microscope objective is imaged in the distance  $z_{MO}$ . Denoting  $f_{MO}$  the microscope objective focal length the quantities are linked with an equation

$$\frac{1}{\Delta z' + f_{MO}} + \frac{1}{z_{MO}} = \frac{1}{f_{MO}}. \quad (4.2)$$

In the Vortex mask plane was created a spherical wave. The complex amplitude of the wave is described with an equation:

$$u(x, y, z) = e^{ikR} = e^{\pm ik\sqrt{x^2+y^2+(z-z_{VM})^2}}, \quad (4.3)$$

$R$  is the radius of the spherical wave and  $z_{VM} = 300$  mm is the position of the vortex mask from the objective. The wave is modified by the vortex mask, which has eight segments in each zone. Such a mask is suitable for manufacturing and previous experiments have shown, that using eight segments should give good results [54].

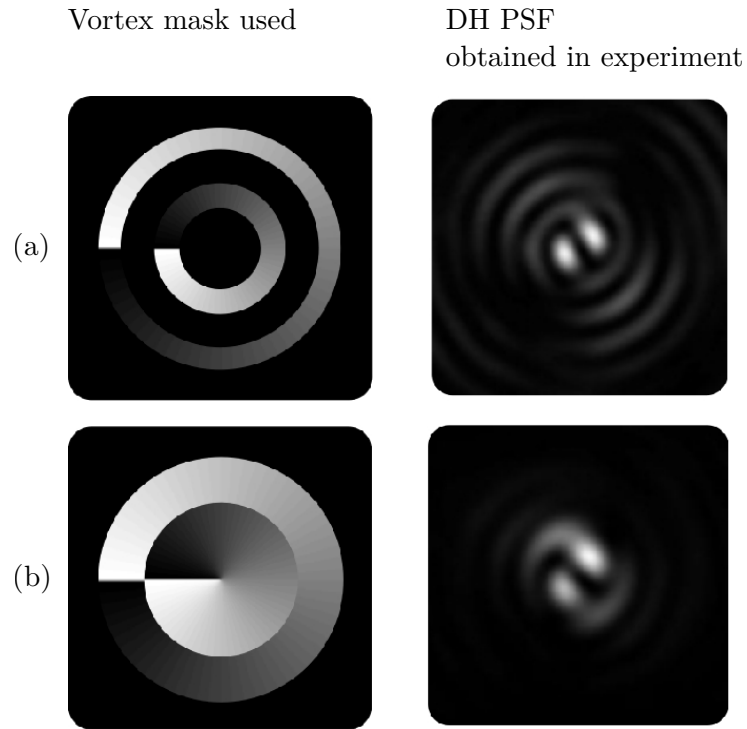


Figure 4.4: Types of vortex masks used and DH PSFs obtained with the masks. (a) Mask realized with thin ring zones. (b) Mask realized with two wide zones. Adopted from [54].

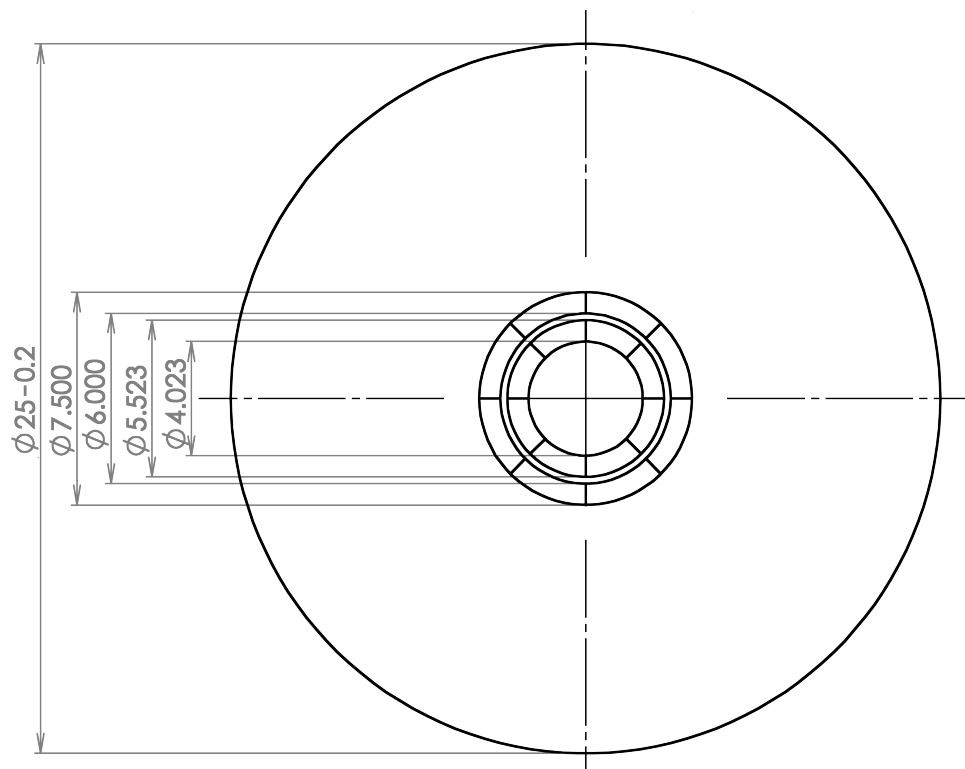


Figure 4.5: Drawing of the vortex mask.

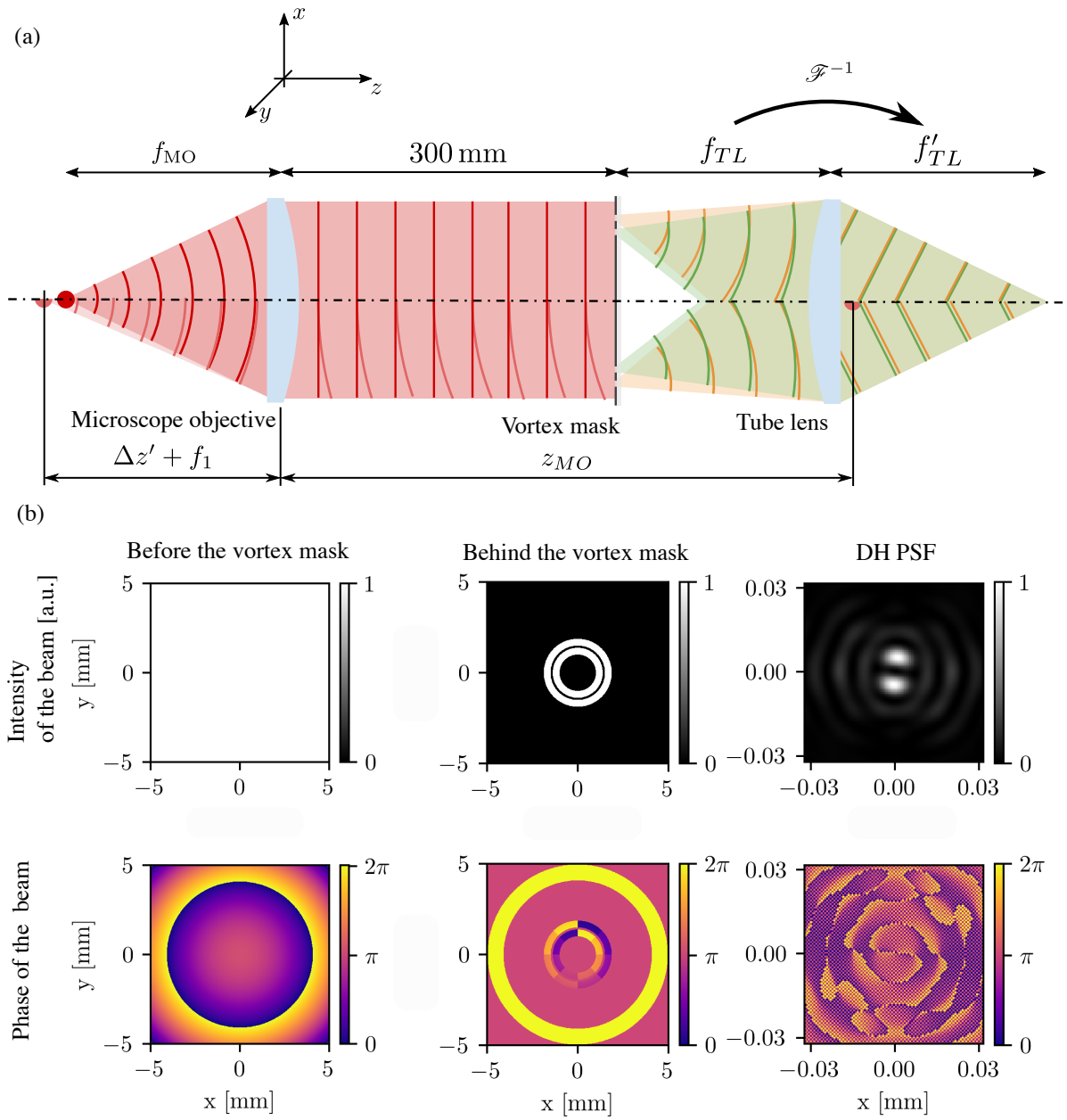


Figure 4.6: Simulation of the mask behavior. (a) Scheme of the setup for the calculations. (b) Fields in parts of the setup.

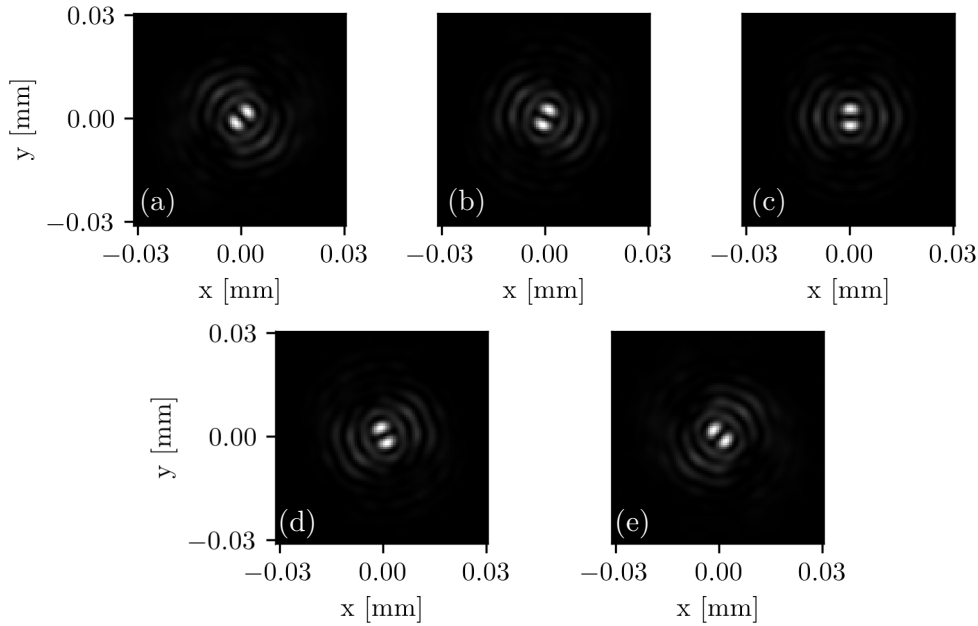


Figure 4.7: Simulation results for the Nikon Plan 10 microscope objective,  $f_{MO} = 20$  mm. Intensity of the DH PSF with the defocuses  $\Delta z'$  from  $-30 \mu\text{m}$  to  $30 \mu\text{m}$  with step  $15 \mu\text{m}$  between the images.

The DH PSF we obtain with an inverse Fourier transform of the complex amplitude wave passed through the vortex mask. The intensity  $I$  is proportional to the squared modulus of the complex amplitude  $u$ :

$$I(x, y) \sim u^2(x, y). \quad (4.4)$$

I did the computation using the Numpy package [55] for creating the array of the complex amplitude in the mask plane. The array is sampled from  $-20$  mm to  $20$  mm with step  $0.01$  mm. The array is multiplied by the mask and an inverse Fourier transform is made. For this step is used the Scipy library [56]. From the result I calculated the intensity in which we may see the DH PSF. The results were plotted with the Matplotlib library [57]. The simulation was done for the wavelength  $\lambda = 810$  nm. Code may be found in the supplementary material.

The results of the simulation may be found in the figures 4.7 and 4.8. The DH PSF rotates with the defocusation. Also if we consider the camera sensor pixel size  $1.5 \mu\text{m}$  [52], the DH PSF should be well resolvable with the Raspberry Pi HQ camera.

### 4.3 Vortex mask fabrication

The mask was fabricated by the group of assoc. prof. Kolařík at the Institute of the Scientific Instruments of the Czech Academy of Sciences. Part of the fabrication was done at the CEITEC Nano facility. The mask consists of three layers as may be seen in the figure 4.9. First is the substrate on the substrate chromium amplitude layer was made. On top of that, the phase layer from PMMA was made.

As the substrate was used  $1$  mm thick and  $25$  mm in diameter High Efficiency Window [58]. The substrate was chosen as the windows were available in the laboratory and the

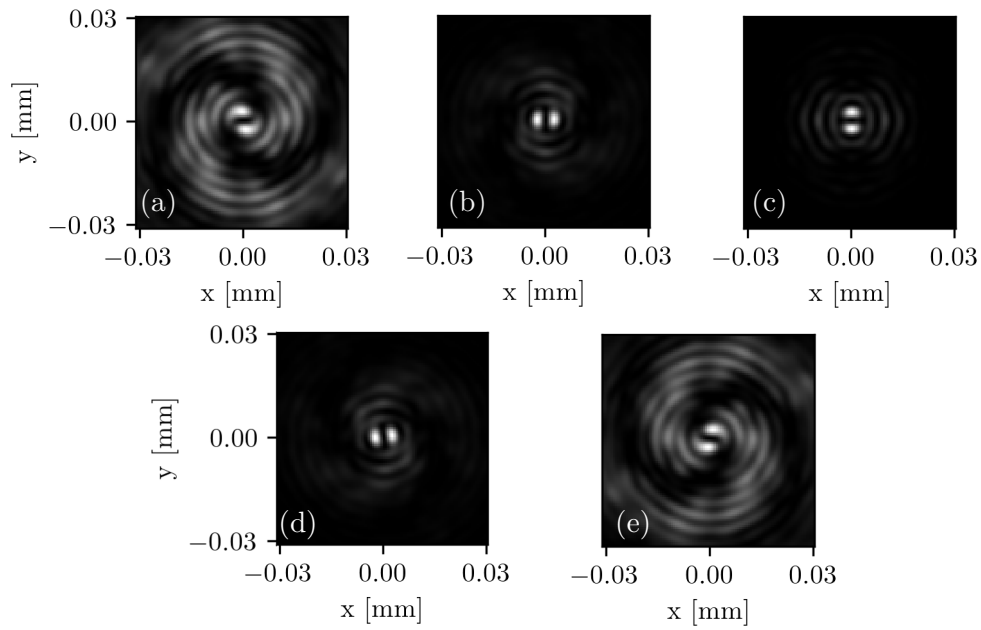


Figure 4.8: Simulation results for the Nikon Plan Fluor 20 microscope objective,  $f_{MO} = 10$  mm. Intensity of the DH PSF with the defocuses  $\Delta z'$  from  $-30 \mu\text{m}$  to  $30 \mu\text{m}$  with step  $15 \mu\text{m}$  between the images.

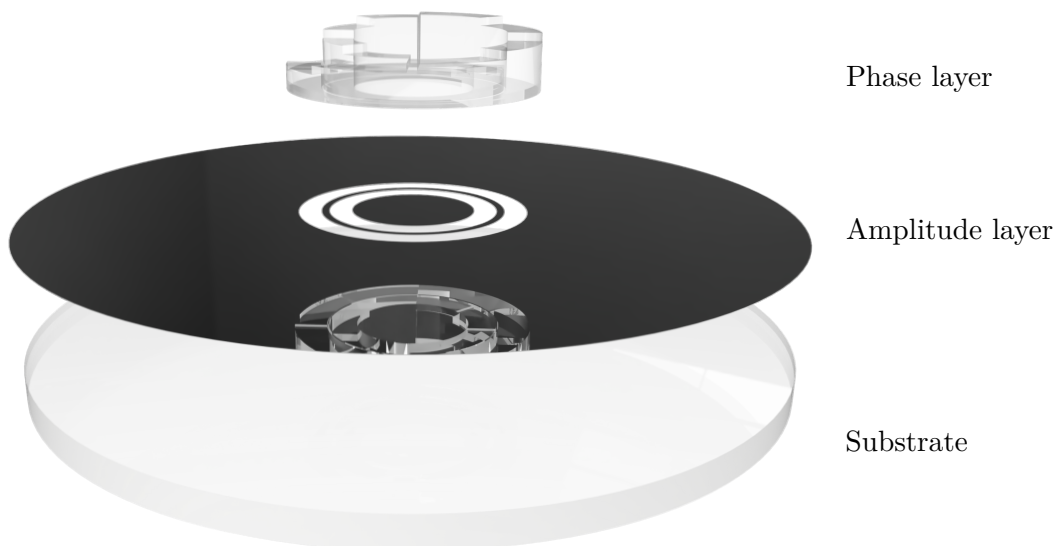


Figure 4.9: Mask structure.

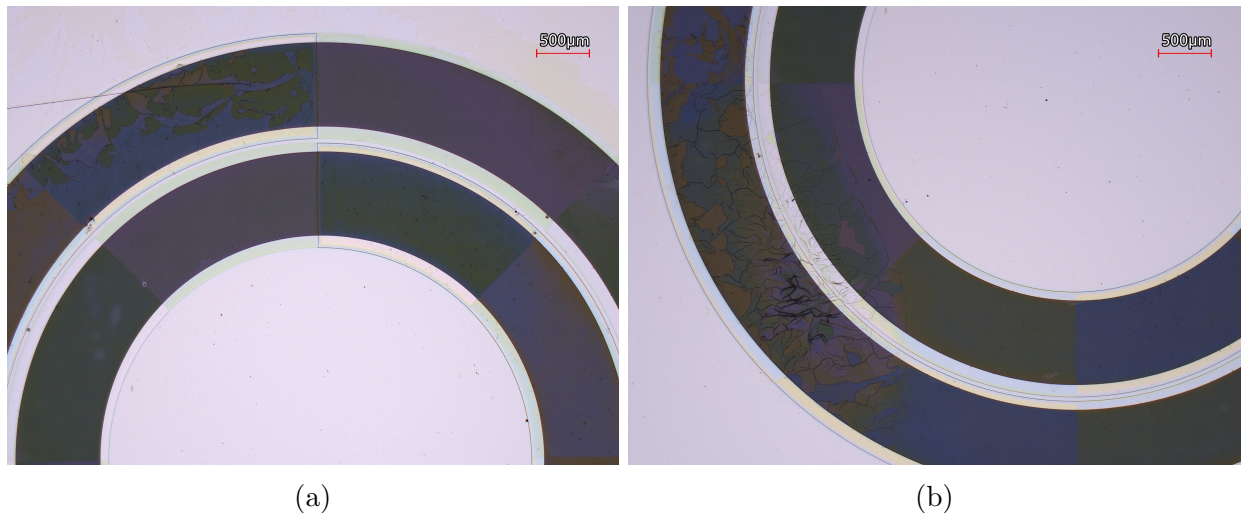


Figure 4.10: The Vortex mask defects photographed with a microscope. Images provided by Ing. Krátký.

surfaces are well polished with good parallelism. The substrate underwent solvent cleaning in the ultrasound cleaner. The surface was then activated using the Diener plasma cleaner [59].

The chromium amplitude layer was sputtered on top of the substrate. The deposition was made with the BESTEC UHV physical vapor deposition system for thin-film e-beam deposition [59]. With this 150 nm thick layer was deposited. As a next step photoresist AZ 1518 [60] was spin-coated. The resist was exposed with photolithograph. The layer was developed using the AZ 726 MIF developer [61] and washed. The rings in chromium were etched using Technietch Cr01 etcher [62]. The rest of the photoresist was stripped to have just substrate with the amplitude layer.

On top of the chromium amplitude layer a PMMA layer was spincoated. The PMMA was exposed using the electron beam lithograph Raith EBPG500. The depth of each segment is in the table (tabulka bude!). Afterwards the mask developed in the mixture of methyl isobutyl ketone and isopropyl alcohol.

The mask was measured using KLA-Tencor AlphaStep D-120 profilometer [63]. The step between the first and eight zone was measure as  $(471 \pm 8)$  nm by the outer zone and  $(464 \pm 4)$  nm by the inner zone. However, the mask was fabricated with the defects which may be seen in the figure 4.10. The defects were caused by the unclean surface of the substrate.

## 4.4 Optomechanics

To align the setup it is needed to use proper optomechanical components, which would allow the fine adjustments. The use of the optomechanical components is also illustrated in the figure 4.2 with the components listed in the table 4.2 [49, 53]. For mounting the dichroic mirror and coverslip with a coverslip I've designed custom holders. The render of the holders may be found in the figure 4.11. The holders were printed with a 3D printer.

To precisely collimate the beam it is important to finely adjust the distance between the collimator and the fiber, therefore the fiber is mounted in the z-stage. Placing the dichroic mirror on the kinematic mount is also crucial so the beam is reflected at the correct angle into the microscope objective. The microscope objective also needs to be centered, so the

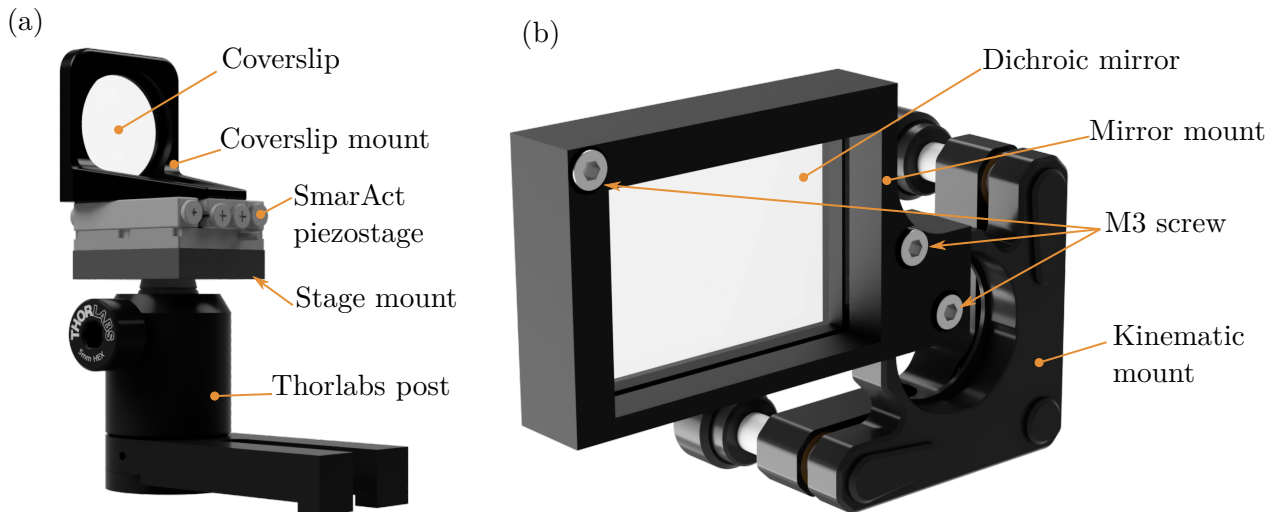


Figure 4.11: Render of custom made parts for the laboratory setup. Popisky budou!

image of the point source is created on the optical axis. The microscope slide is mounted on the piezo stage. The use of the piezo stage is important as it can move with 100 nm precision, so the module can be tested. The mirror in the imaging part is also mounted in the kinematic mechanism. The mechanism with an x-y stage together are used to center the mask within the imaging part.

The design of the setup became a base for its realization.

# 5 Experiments

In the previous chapter, the design and simulations of the setup have been discussed. In this chapter I describe how the design has been implemented and tested.

## 5.1 Alignment

For building the setup Thorlabs cage system [49] have been used. The parts have been aligned as the light propagates along the optical pathway.

- First the fiber was collimated. For collimation, a combination of Nikon Plan 10 microscope objective and Raspberry PI camera have been used. The objective and the camera have been properly aligned using the plane wave created by the HeNe laser ( $\lambda = 632.8 \text{ nm}$ ), so the spot observed in the camera has a minimal diameter. Such aligned camera and microscope objective were used to observe how collimated the beam is. The collimator was placed in the proper position and then the position of the fiber was finely adjusted. The objective with the camera were afterward removed.
- Secondly was aligned the dichroic mirror in combination with microscope objective. The camera have been placed instead the coverslip. The camera was deliberately out of focus and the dichroic mirror with the microscope objective were adjusted to ensure that the whole beam fits into the aperture stop of the microscope objective. This was used as if the beam did not fit in the camera was not observed circular spot.
- As third were aligned the tube lens in combination with the mask and camera. For the adjustment were used the plane wave created by the HeNe laser. Both the camera and mask were placed in a plane with the smallest spot. The mask was mounted in the small tube. The tube was mounted in the x-y stage, so the mask could be easily disassembled.
- In the fourth step the aligned imaging part was added to the rest of the system. The mask was disassembled and the coverslip was placed into the working distance of the microscope objective. The point observed in the camera was centered with the tilt of the mirror.
- Finally the mask was centered so the DH PSF observed in the camera would have both blobs equally big.

## 5.2 Control software

For controlling the experiment have been written a Python script. The script was running on the Raspberry Pi 4 (8 GB RAM version) computer running the Raspberry Pi OS [50]. The computer has been communicating with the SmarAct piezo stage via serial line commands as

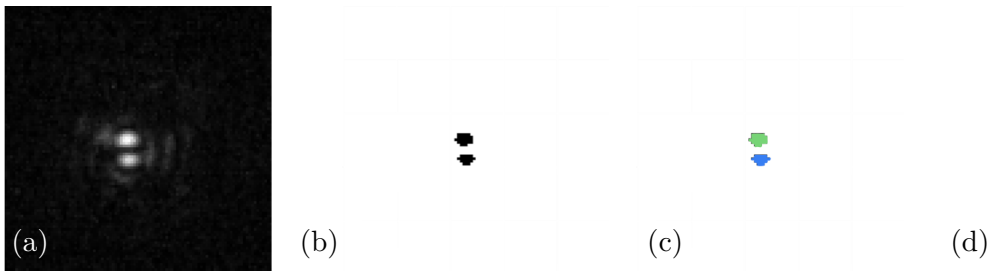


Figure 5.1: Image processing visualisation. (a) Captured image. (b) Threshold. (c) Segmentation. (d) Centre of masses computation.

the manufacturer enables [53]. I programmed the python functions which then were sending the commands via the pySerial library [64]. The images have been acquired with the libcamera program, which has been called via the terminal. The script with the functions may be found in the supplementary material.

### 5.3 Image processing

To measure the angle of rotation of the DH PSF I have written a Python script. The script uses image segmentation to find the individual blobs and calculates their positions. The angle is calculated from the positions of the blobs. The detailed description of the program follows the figure 5.1.

- The image is loaded as a Numpy array
- The image is thresholded into the binary mask. For each of the RGB channels, a different threshold is chosen.
- Using the `label` function from the Scipy ndpackage, the blobs are segmented [56].
- The centers of masses of each blob are found with the `center_of_mass` function from the Scipy ndpackage [56].
- The angle of the line given by those two points is calculated using the `arctan2` function from the Numpy library [55].

### 5.4 Experiments

The setup has been aligned as described earlier in section 5.1 for both objective lenses. However, it was hard to do proper alignment and the DH PSF on the camera. Even if the DH PSF was found, there were ghosts, as may be seen in the figure 5.2, the setup was programmed to scan with the coverslip along the axis.

Using the Nikon Plan 10 objective the coverslip is moved to a position, which seemed to be in focus, and scanned in range  $\pm 20 \mu\text{m}$  with a step  $0.2 \mu\text{m}$  capturing position and image from the camera at each point. The scan was repeated eight times. After processing the images as described, the results may be found in the figure 5.3. Filtering the data and taking just those which are plotted in blue ( $z < 15 \mu\text{m}$ ).

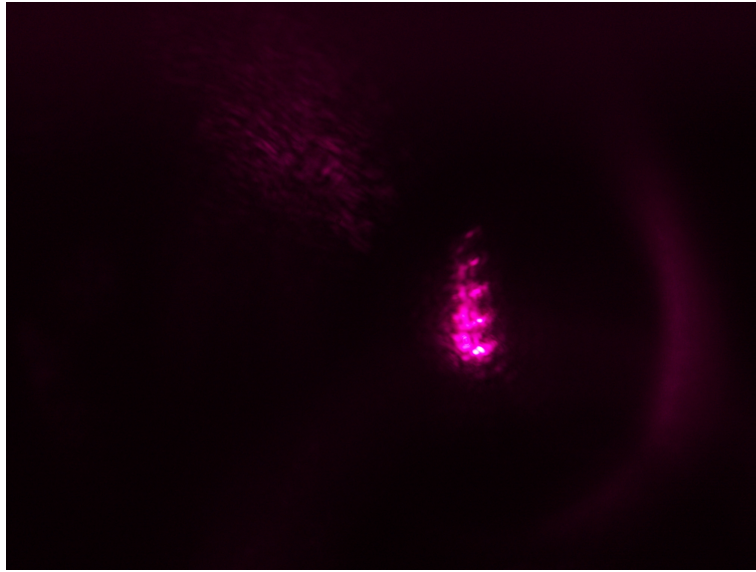


Figure 5.2: The image obtained from the camera, while doing the experiment with Nikon Plan 10 lens. In the figure are two bright blobs of the DH PSF.

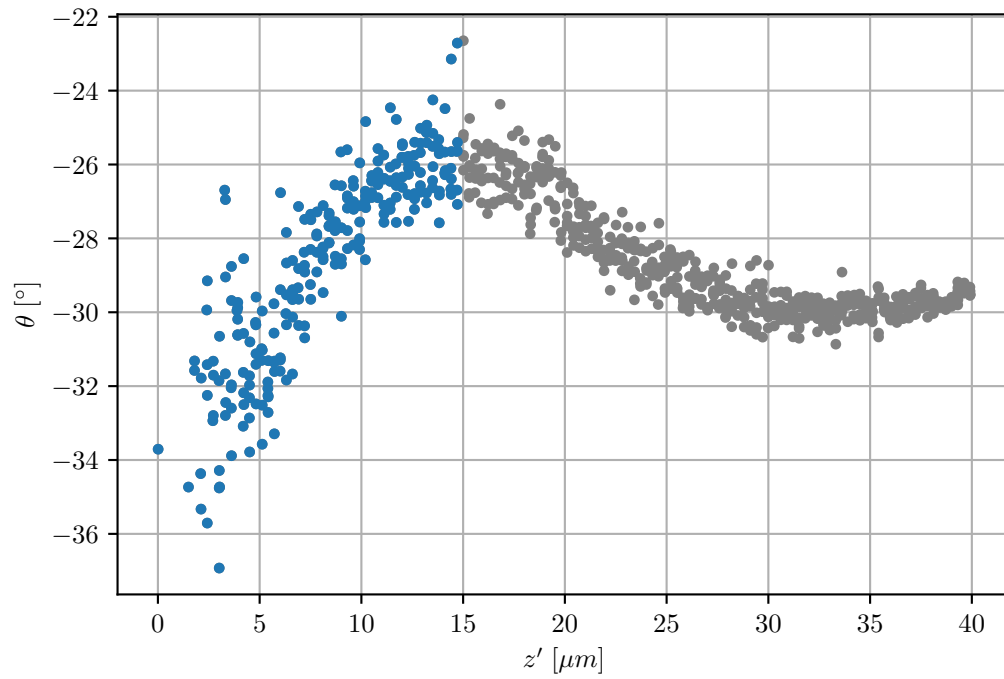


Figure 5.3: Results of the measurement with Nikon Plan 10 objective.

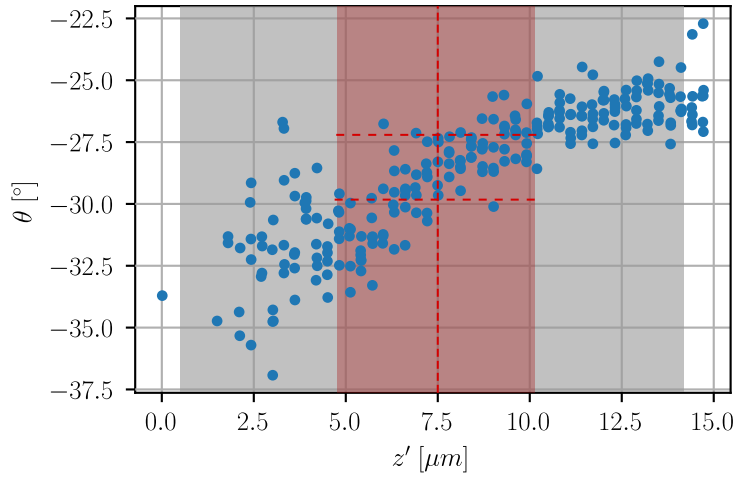


Figure 5.4: Filtered results of the measurement with Nikon Plan 10 objective. The gray rectangle illustrates the depth of focus, which is  $\pm 6.8 \mu\text{m}$ . The red zones illustrates the detection precision  $\pm 2.6 \mu\text{m}$ .

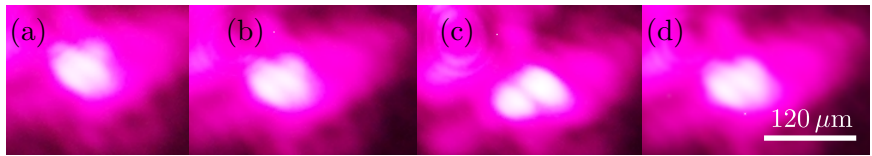


Figure 5.5: Results of the measurement with Nikon Plan 10 objective. Axial positions  $z'$  from (a) to (d):  $2.12 \mu\text{m}$ ,  $4.5 \mu\text{m}$ ,  $8.12 \mu\text{m}$ ,  $11.7 \mu\text{m}$ . DH PSF angle  $\theta$  from (a) to (d):  $-35.32^\circ$ ,  $-31.7^\circ$ ,  $-29.46^\circ$ ,  $-24.7^\circ$ .

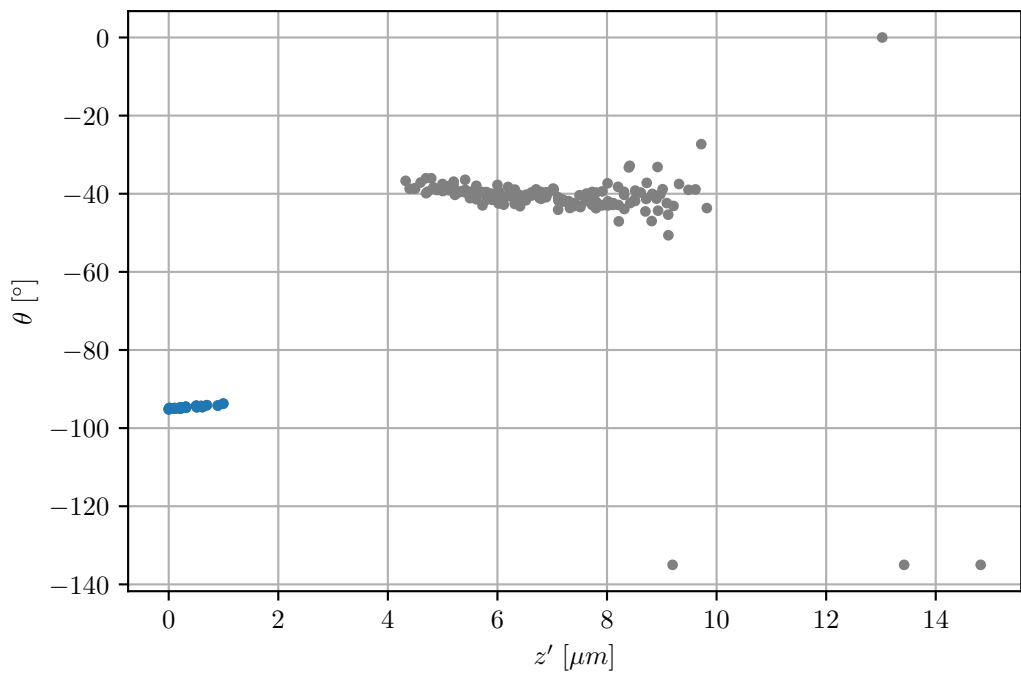


Figure 5.6: Results of the measurement with Nikon Plan 20 objective.

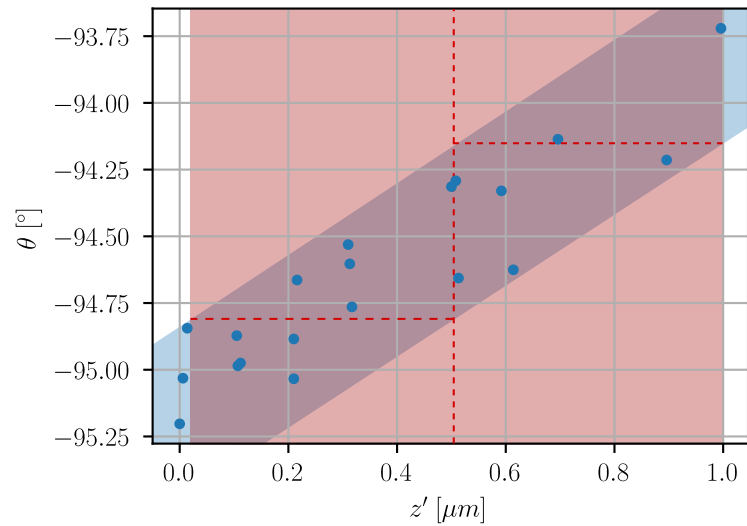


Figure 5.7: Filtered results of the measurement with Nikon Plan 20 objective. There have been drawn the blue stripe around the points to find the red detection precision, which is  $\pm 0.5 \mu m$ . The depth of field is  $\pm 1.7 \mu m$

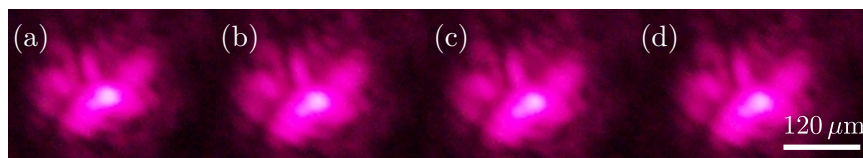


Figure 5.8: Results of the measurement with Nikon Plan Fluor 20 objective. Axial positions  $z'$  from (a) to (d):  $0.01 \mu m$ ,  $0.22 \mu m$ ,  $0.70 \mu m$ ,  $1.00 \mu m$ . DH PSF angle  $\theta$  from (a) to (d):  $-95.0^\circ$ ,  $-94.6^\circ$ ,  $-94.13^\circ$ ,  $-93.72^\circ$ .

The filtered data are in the figure 5.4. Here we can see that if we take the range of angles for each position, we still can detect change in axial position up to  $\pm 2.6 \mu\text{m}$ . Which is safely within the depth of field. The Nikon Plan 10 has the depth of field  $\pm 6.8 \mu\text{m}$ .

Repeating the experiment with the Nikon Plan Fluor 20 objective lens. Using this lens I scanned in the range  $\pm 5 \mu\text{m}$  around the point which seemed to be in focus. The results may be found in the figure 5.6. The data were filtered and the results after filtering are in the figure 5.7. From the plot it is clear that more data would be needed to collect, to reliably determine the precision. However, if we look into the data, we can see, that they lie in a stripe. If we handle the stripe same as the data in the figure 5.4 we can obtain, that the method should be able to safely detect movement  $\pm 0.5 \mu\text{m}$  along the axis. As the depth of field is  $\pm 1.7 \mu\text{m}$ .

In both cases is the detection precision lower than the depth of field. Therefore the setup is suitable for maintaining the sample in focus.

Fitting the data with a line, we obtained that the coefficient  $K$  giving the relation between defocus and rotation

$$K = \frac{\Delta\theta}{\Delta z'}.$$

From the data in the figure 5.4 we obtain  $K_{10} = (0.61 \pm 0.02)^\circ/\mu\text{m}$  for the Nikon Plan 10. Applying the same on the data in the figure 5.7 we obtain  $K_{20} = (1.16 \pm 0.12)^\circ/\mu\text{m}$ . Those constants will be important for creating the algorithm with feedback loop, which is maintaining the image in focus.

As was mentioned before the experiment was done to prove the concept and kalibrate the constants  $K_{10}$  and  $K_{20}$ . Unfortunately I was not able to get DH PSF in qualities as have been published [43, 54]. The results were probably caused due the defects in the mask. Unfortunately the mask manufacturing is long lasting process. Therefore there was not enough time to repeat the experiment with properly manufactured mask.

Further experiments needs to be carried out to properly test the module. With properly fabricated mask a long term experiment can be done. For this experiment a program with feedback loop is written and may be found in the supplementary material.

In the program user sets the position of the sample and the program captures the angle of the DH PSF. Using the constant  $K$  obtained in the calibration. During the experiment the module captures DH PSF, compares its position to the initial one. If the movement corresponding to the DH PSF is bigger than some threshold, the sample position is corrected. The program may be found in the supplementary material.

## Summary

The measured data presented in the previous chapter have shown the potential, of this method, as the precision of localisation is in both cases much lower than the depth of focus. Further experiments needs to be carried out.

I have successfully designed a hardware autofocus. The designed system is smaller as those in previously used experiments. Ommiting the  $4f$  system meant miniaturisation of the module, so it is small enough to be inbuilt into the microscope. I have build and aligned the laboratory setup of the module. The mask have been designed. I have simulated the behavior of the mask with a Python script. The mask have been fabricated and mounted into the setup. Even though, the mask have been fabricated with defects, I was able to carry out measurments with ten and twenty times magnifying objective lens. Unfortunately just with properly fabricated mask a long term experiment can be done. For such a experiment I have designed a software with the feedback loop. So the module can be tested during a long term observation. The proven concept should also be also tested using 40-times and 60-times microscope objectives, as they have shallow depth of focus.



# Bibliography

1. BORN, Max; WOLF, Emil. *Principles of Optics: 60th Anniversary Edition*. Cambridge University Press, 2019. ISBN 9781108769914. Available from DOI: 10.1017/9781108769914.
2. GOULETTE, Travis; HOWARD, Charles D.; DAVIDSON, Michael W. *Infinity Optical Systems* [online]. Nikon Instruments Inc., 2021 [visited on 2021-12-30]. Available from: <https://www.microscopyu.com/microscopy-basics/infinity-optical-systems>.
3. CHANDLER, Douglas E.; ROBERSON, Robert W. *Bioimaging : current concepts in light and electron microscopy*. Jones and Bartlett Publishers, 2009. ISBN 0763738743. Available also from: <https://books.google.com/books/about/Bioimaging.html?id=dqP8FCEiMGgC>.
4. ABBE, Ernst. Beiträge zur Theorie des Mikroskops und der mikroskopischen Wahrnehmung. *Archiv für Mikroskopische Anatomie 1873 9:1*. 1873, vol. 9, pp. 413–468. ISSN 01767364. Available from DOI: 10.1007/BF02956173.
5. MARTIMER, Abramowitz; W., Davidson Michael. *Specialized Microscopy Techniques - Darkfield Illumination — Olympus LS* [online]. Olympus corporation, [n.d.] [visited on 2021-02-11]. Available from: <https://www.olympus-lifescience.com/en/microscope-resource/primer/techniques/darkfield/>.
6. ZERNIKE, F. Phase contrast, a new method for the microscopic observation of transparent objects. *Physica*. 1942, vol. 9, pp. 686–698. ISSN 0031-8914. Available from DOI: 10.1016/S0031-8914(42)80035-X.
7. ZERNIKE, F. Phase contrast, a new method for the microscopic observation of transparent objects part II. *Physica*. 1942, vol. 9, pp. 974–986. ISSN 0031-8914. Available from DOI: 10.1016/S0031-8914(42)80079-8.
8. MURPHY, Douglas B.; OLDFIELD, Ron; SCHWARTZ, Stanley; DAVIDSON, Michael W. *Introduction to Phase Contrast Microscopy* [online]. Nikon Instruments Inc., 2022 [visited on 2022-02-06]. Available from: <https://www.microscopyu.com/techniques/phase-contrast/introduction-to-phase-contrast-microscopy>.
9. ROBINSON, Philip C.; DAVIDSON, Michael W. *Polarized Light Microscopy* [online]. Nikon Instruments Inc., 2022 [visited on 2021-02-11]. Available from: <https://www.microscopyu.com/techniques/polarized-light/polarized-light-microscopy>.
10. ALLEN, R. D.; DAVID, G. B.; NOMARSKI, G. The zeiss-Nomarski differential interference equipment for transmitted-light microscopy. *Zeitschrift für wissenschaftliche Mikroskopie und mikroskopische Technik*. 1969, vol. 69, pp. 193–221. ISSN 0373031X.
11. DUNCAN, Donald D.; FISCHER, David G.; DAYTON, Amanda; PRAHL, Scott A. Quantitative Carré differential interference contrast microscopy to assess phase and amplitude. *Journal of the Optical Society of America A*. 2011, vol. 28, p. 1297. ISSN 1084-7529. Available from DOI: 10.1364/JOSAA.28.001297.

12. PATTERSON, George; DAY, Rich N.; PISTON, David. Fluorescent protein spectra. *Journal of Cell Science*. 2001, vol. 114, pp. 837–838. ISSN 1477-9137. Available from DOI: [10.1242/jcs.114.5.837](https://doi.org/10.1242/jcs.114.5.837).
13. ETTINGER, Andreas; WITTMANN, Torsten. Fluorescence live cell imaging. *Methods in Cell Biology*. 2014, vol. 123, pp. 77–94. ISSN 0091-679X. Available from DOI: [10.1016/B978-0-12-420138-5.00005-7](https://doi.org/10.1016/B978-0-12-420138-5.00005-7).
14. R., Spring Kenneth; W., Davidson Michael. *Introduction to Fluorescence Microscopy — Nikon's MicroscopyU* [online]. Nikon Instruments Inc., 2022 [visited on 2022-02-18]. Available from: <https://www.microscopyu.com/techniques/fluorescence/introduction-to-fluorescence-microscopy>.
15. PARK, Yong Keun; DEPEURSINGE, Christian; POPESCU, Gabriel. Quantitative phase imaging in biomedicine. *Nature Photonics* 2018 12:10. 2018, vol. 12, pp. 578–589. ISSN 1749-4893. Available from DOI: [10.1038/s41566-018-0253-x](https://doi.org/10.1038/s41566-018-0253-x).
16. LIPPINCOTT-SCHWARTZ, Jennifer; PATTERSON, George H. Development and Use of Fluorescent Protein Markers in Living Cells. *Science*. 2003, vol. 300, pp. 87–91. ISSN 0036-8075. Available from DOI: [10.1126/science.1082520](https://doi.org/10.1126/science.1082520).
17. HELL, Stefan W.; WICHMANN, Jan. Breaking the diffraction resolution limit by stimulated emission: stimulated-emission-depletion fluorescence microscopy. *Optics Letters* [online]. 1994, vol. 19, no. 11, pp. 780–782 [visited on 2022-03-30]. ISSN 1539-4794. Available from DOI: [10.1364/OL.19.000780](https://doi.org/10.1364/OL.19.000780). Publisher: Optica Publishing Group.
18. BETZIG, Eric; PATTERSON, George H.; SOUGRAT, Rachid; LINDWASSER, O. Wolf; OLENYCH, Scott; BONIFACINO, Juan S.; DAVIDSON, Michael W.; LIPPINCOTT-SCHWARTZ, Jennifer; HESS, Harald F. Imaging Intracellular Fluorescent Proteins at Nanometer Resolution. *Science* [online]. 2006, vol. 313, no. 5793, pp. 1642–1645 [visited on 2022-03-30]. Available from DOI: [10.1126/science.1127344](https://doi.org/10.1126/science.1127344). Publisher: American Association for the Advancement of Science.
19. HESS, Samuel T.; GIRIRAJAN, Thanu P. K.; MASON, Michael D. Ultra-High Resolution Imaging by Fluorescence Photoactivation Localization Microscopy. *Biophysical Journal* [online]. 2006, vol. 91, no. 11, pp. 4258–4272 [visited on 2022-03-30]. ISSN 0006-3495. Available from DOI: [10.1529/biophysj.106.091116](https://doi.org/10.1529/biophysj.106.091116).
20. RUST, Michael J.; BATES, Mark; ZHUANG, Xiaowei. Sub-diffraction-limit imaging by stochastic optical reconstruction microscopy (STORM). *Nature Methods* [online]. 2006, vol. 3, no. 10, pp. 793–796 [visited on 2022-03-30]. ISSN 1548-7105. Available from DOI: [10.1038/nmeth929](https://doi.org/10.1038/nmeth929). Number: 10 Publisher: Nature Publishing Group.
21. BALZAROTTI, Francisco; EILERS, Yvan; GWOSCH, Klaus C.; GYNNÅ, Arvid H.; WESTPHAL, Volker; STEFANI, Fernando D.; ELF, Johan; HELL, Stefan W. Nanometer resolution imaging and tracking of fluorescent molecules with minimal photon fluxes. *Science* [online]. 2017, vol. 355, no. 6325, pp. 606–612 [visited on 2022-03-30]. ISSN 0036-8075, ISSN 1095-9203. Available from DOI: [10.1126/science.aak9913](https://doi.org/10.1126/science.aak9913).
22. STEPHENS, David J.; ALLAN, Victoria J. Light microscopy techniques for live cell imaging. *Science*. 2003, vol. 300, pp. 82–86. ISSN 00368075. Available from DOI: <https://doi.org/10.1126/science.1082160>.
23. JENSEN, Ellen C. Overview of Live-Cell Imaging: Requirements and Methods Used. *The Anatomical Record: Advances in Integrative Anatomy and Evolutionary Biology*. 2013, vol. 296, pp. 1–8. ISSN 19328486. Available from DOI: [10.1002/ar.22554](https://doi.org/10.1002/ar.22554).

24. BAKER, Monya. Taking a long, hard look. *Nature* 2010 466:7310. 2010, vol. 466, pp. 1137–1138. ISSN 1476-4687. Available from DOI: 10.1038/4661137a.
25. SHAH, M.i.; MISHRA, S.; SARKAR, M.; ROUT, C. Identification of robust focus measure functions for the automated capturing of focused images from Ziehl–Neelsen stained sputum smear microscopy slide. *Cytometry Part A* [online]. 2017, vol. 91, no. 8, pp. 800–809 [visited on 2022-04-05]. ISSN 1552-4930. Available from DOI: 10.1002/cyto.a.23142. \_eprint: <https://onlinelibrary.wiley.com/doi/pdf/10.1002/cyto.a.23142>.
26. MASON, D. C.; GREEN, D. K. Automatic Focusing of a Computer-Controlled Microscope. *IEEE Transactions on Biomedical Engineering* [online]. 1975, vol. BME-22, no. 4, pp. 312–317 [visited on 2022-04-03]. ISSN 0018-9294. Available from DOI: 10.1109/TBME.1975.324450.
27. MENDELSON, Mortimer L.; MAYALL, Brian H. Computer-Oriented analysis of human chromosomes—III. Focus. *Computers in Biology and Medicine* [online]. 1972, vol. 2, no. 2, pp. 137–150 [visited on 2022-04-03]. ISSN 0010-4825. Available from DOI: 10.1016/0010-4825(72)90044-3.
28. BRENNER, J F; DEW, B S; HORTON, J B; KING, T; NEURATH, P W; SELLES, W D. An automated microscope for cytologic research a preliminary evaluation. *Journal of Histochemistry & Cytochemistry* [online]. 1976, vol. 24, no. 1, pp. 100–111 [visited on 2022-04-05]. ISSN 0022-1554, ISSN 1551-5044. Available from DOI: 10.1177/24.1.1254907.
29. LANG, Walter. *Vorrichtung zur automatischen Fokussierung von Mikroskopen*. Pat., DE2008390. 1976-03 [visited on 2022-04-05]. Available from: <https://register.dpma.de/DPMAreger/pat/PatSchrifteneinsicht?docId=DE000002008390C3&page=1&dpi=300&lang=de&full=true>.
30. PERTUZ, Said; PUIG, Domenec; GARCIA, Miguel Angel. Analysis of focus measure operators for shape-from-focus. *Pattern Recognition* [online]. 2013, vol. 46, no. 5, pp. 1415–1432 [visited on 2022-04-05]. ISSN 00313203. Available from DOI: 10.1016/j.patcog.2012.11.011.
31. PINKARD, Henry; PHILLIPS, Zachary; BABAKHANI, Arman; FLETCHER, Daniel A.; WALLER, Laura. Deep learning for single-shot autofocus microscopy. *Optica*. 2019, vol. 6, no. 6, p. 794. ISSN 2334-2536. Available from DOI: 10.1364/optica.6.000794. Publisher: The Optical Society.
32. BIAN, Zichao; GUO, Chengfei; JIANG, Shaowei; ZHU, Jiakai; WANG, Ruihai; SONG, Pengming; ZHANG, Zibang; HOSHINO, Kazunori; ZHENG, Guoan. Autofocusing technologies for whole slide imaging and automated microscopy. *Journal of Biophotonics* [online]. 2020, vol. 13, no. 12 [visited on 2022-04-11]. ISSN 1864-063X, ISSN 1864-0648. Available from DOI: 10.1002/jbio.202000227.
33. LIRON, Y.; PARAN, Y.; ZATORSKY, N. G.; GEIGER, B.; KAM, Z. Laser autofocus-ing system for high-resolution cell biological imaging. *Journal of Microscopy* [online]. 2006, vol. 221, no. 2, pp. 145–151 [visited on 2022-05-20]. ISSN 1365-2818. Available from DOI: 10.1111/j.1365-2818.2006.01550.x. \_eprint: <https://onlinelibrary.wiley.com/doi/pdf/10.1111/j.1365-2818.2006.01550.x>.
34. *Nikon Perfect Focus System (PFS)* [online]. [N.d.] [visited on 2022-05-20]. Available from: <https://www.microscopyu.com/applications/live-cell-imaging/nikon-perfect-focus-system>.

35. REINHEIMER, G. *Arrangement for automatically focussing an optical instrument*. Pat., US3721827A. 1973-03 [visited on 2022-05-20]. Available from: <https://patents.google.com/patent/US3721827A/en>.
36. VIRAG, Tibor; LASZLO, Attila; MOLNAR, Bela; TAGSCHERER, Attila; VARGA, Viktor Sebestyén. *Focusing Method for the High-Speed Digitalisation of Microscope Slides and Slide Displacing Device, Focusing Optics, and Optical Rangefinder*. Pat., US20080099661A1. 2008-05 [visited on 2022-05-20]. Available from: <https://patents.google.com/patent/US20080099661/en>.
37. ZOU, Yunlu; CRANDALL, Greg J.; OLSON, Allen. *Real-time focusing in line scan imaging*. Pat., US9841590B2. 2017-12 [visited on 2022-05-20]. Available from: <https://patents.google.com/patent/US9841590B2/en>.
38. OLSON, Allen; SALIGRAMA, Kiran; ZOU, Yunlu; NAJMABADI, Peyman. *Real-time autofocus focusing algorithm*. Pat., US10459193B2. 2019-10 [visited on 2022-05-20]. Available from: <https://patents.google.com/patent/US10459193B2/en?q=US10%2c459%2c193>.
39. GUO, Kaikai; LIAO, Jun; BIAN, Zichao; HENG, Xin; ZHENG, Guoan. InstantScope: a low-cost whole slide imaging system with instant focal plane detection. *Biomedical Optics Express* [online]. 2015, vol. 6, no. 9, pp. 3210–3216 [visited on 2022-05-20]. ISSN 2156-7085. Available from DOI: 10.1364/BOE.6.003210. Publisher: Optica Publishing Group.
40. GREENGARD, Adam; SCHECHNER, Yoav Y.; PIESTUN, Rafael. Depth from diffracted rotation. *Optics Letters*. 2006, vol. 31, no. 2, p. 181. ISSN 0146-9592. Available from DOI: 10.1364/ol.31.000181.
41. PAVANI, Sri Rama Prasanna; PIESTUN, Rafael. High-efficiency rotating point spread functions. *Optics Express*. 2008, vol. 16, no. 5, p. 3484. ISSN 1094-4087. Available from DOI: 10.1364/oe.16.003484.
42. WANG, Zhaojun; CAI, Yanan; LIANG, Yansheng; ZHOU, Xing; YAN, Shaohui; DAN, Dan; BIANCO, Piero R.; LEI, Ming; YAO, Baoli. Single shot, three-dimensional fluorescence microscopy with a spatially rotating point spread function. *Biomedical Optics Express*. 2017, vol. 8, no. 12, p. 5493. ISSN 2156-7085. Available from DOI: 10.1364/boe.8.005493.
43. BOUCHAL, Petr; BOUCHAL, Zdeněk. Flexible non-diffractive vortex microscope for three-dimensional depth-enhanced super-localization of dielectric, metal and fluorescent nanoparticles. *Journal of Optics (United Kingdom)*. 2017, vol. 19, no. 10. ISSN 20408986. Available from DOI: 10.1088/2040-8986/aa87fb.
44. ICHA, Jaroslav; WEBER, Michael; WATERS, Jennifer C.; NORDEN, Caren. Phototoxicity in live fluorescence microscopy, and how to avoid it. *BioEssays*. 2017, vol. 39, no. 8, pp. 1–15. ISSN 15211878. Available from DOI: 10.1002/bies.201700003.
45. LIU, Y; CHENG, D K; SONEK, G J; BERNS, M W; TROMBERG, B J. Microfluorometric technique for the determination of localized heating in organic particles. *Appl. Phys. Lett.* 1994, vol. 65, p. 919. Available from DOI: 10.1063/1.112981.
46. MASTERS, Barry R; SO, Peter T C; BUEHLER, Christof; BARRY, Nicholas; SUTIN, Jason D; MANTULIN, William W; GRATTON, Enrico. Mitigating thermal mechanical damage potential during two-photon dermal imaging. 2004. Available from DOI: 10.1117/1.1806135.

47. B, Murphy Douglas; D., Salmon Edward; ABRAMOWITZ, Mortimer; W., Davidson Michael. *Světelné víry — Laboratoř digitální optiky* [online]. Olomouc, 2015 [visited on 2019-02-11]. Available from: [http://ldo.optol.cz/cs/?page\\_id=2711](http://ldo.optol.cz/cs/?page_id=2711).
48. BARÁNEK, Michal; BOUCHAL, Petr; ŠILER, Martin; BOUCHAL, Zdeněk. Aberration resistant axial localization using a self-imaging of vortices. *Optics Express* [online]. 2015, vol. 23, no. 12, p. 15316 [visited on 2022-05-19]. ISSN 1094-4087. Available from DOI: 10.1364/OE.23.015316.
49. THORLABS INC. [online]. 2022 [visited on 2022-05-20]. Available from: <https://www.thorlabs.com>.
50. RASPBERRYPI [online]. 2022 [visited on 2022-05-20]. Available from: <https://www.raspberrypi.com>.
51. NIKON INSTRUMENTS INC. [online]. 2022 [visited on 2022-05-20]. Available from: <https://www.microscope.healthcare.nikon.com>.
52. SONY SEMICONDUCTOR SOLUTIONS CORPORATION. *IMX477 Product information* [online]. 2018 [visited on 2022-05-27]. Available from: [https://www.sony-semicon.co.jp/products/common/pdf/IMX477-AACK\\_Flyer.pdf](https://www.sony-semicon.co.jp/products/common/pdf/IMX477-AACK_Flyer.pdf).
53. SMARACT GMBH. [online]. 2022 [visited on 2022-05-20]. Available from: <https://www.smaract.com/index-en>.
54. PETR, Bouchal. *Correlation and Spiral Microscopy using a Spatial Light Modulation* [online]. Brno, 2016 [visited on 2022-05-28]. Available from: [https://www.vut.cz/www\\_base/zav\\_prace\\_soubor\\_verejne.php?file\\_id=123442](https://www.vut.cz/www_base/zav_prace_soubor_verejne.php?file_id=123442). doctoral thesis. Brno University of Technology.
55. HARRIS, Charles R.; MILLMAN, K. Jarrod; WALT, Stéfan J. van der; GOMMERS, Ralf; VIRTANEN, Pauli; COURNAPEAU, David; WIESER, Eric; TAYLOR, Julian; BERG, Sebastian; SMITH, Nathaniel J.; KERN, Robert; PICUS, Matti; HOYER, Stephan; KERKWIJK, Marten H. van; BRETT, Matthew; HALDANE, Allan; RÍO, Jaime Fernández del; WIEBE, Mark; PETERSON, Pearu; GÉRARD-MARCHANT, Pierre; SHEPPARD, Kevin; REDDY, Tyler; WECKESSER, Warren; ABBASI, Hameer; GOHLKE, Christoph; OLIPHANT, Travis E. Array programming with NumPy. *Nature*. 2020, vol. 585, no. 7825, pp. 357–362. Available from DOI: 10.1038/s41586-020-2649-2.
56. VIRTANEN, Pauli; GOMMERS, Ralf; OLIPHANT, Travis E.; HABERLAND, Matt; REDDY, Tyler; COURNAPEAU, David; BUROVSKI, Evgeni; PETERSON, Pearu; WECKESSER, Warren; BRIGHT, Jonathan; VAN DER WALT, Stéfan J.; BRETT, Matthew; WILSON, Joshua; MILLMAN, K. Jarrod; MAYOROV, Nikolay; NELSON, Andrew R. J.; JONES, Eric; KERN, Robert; LARSON, Eric; CAREY, C J; POLAT, İlhan; FENG, Yu; MOORE, Eric W.; VANDERPLAS, Jake; LAXALDE, Denis; PERKTOLD, Josef; CIMRMAN, Robert; HENRIKSEN, Ian; QUINTERO, E. A.; HARRIS, Charles R.; ARCHIBALD, Anne M.; RIBEIRO, Antônio H.; PEDREGOSA, Fabian; VAN MULBREGT, Paul; SCIPY 1.0 CONTRIBUTORS. SciPy 1.0: Fundamental Algorithms for Scientific Computing in Python. *Nature Methods*. 2020, vol. 17, pp. 261–272. Available from DOI: 10.1038/s41592-019-0686-2.
57. HUNTER, J. D. Matplotlib: A 2D graphics environment. *Computing in Science & Engineering*. 2007, vol. 9, no. 3, pp. 90–95. Available from DOI: 10.1109/MCSE.2007.55.

58. EDMUND OPTICS INC. *25.4mm Dia. x 1mm High Efficiency Window* [online]. 2022 [visited on 2022-05-27]. Available from: <https://www.edmundoptics.com/p/254mm-dia-x-1mm-high-efficiency-window/9280/>.
59. CEITEC NANO FACILITY. *Nanofabrication laboratory equipment* [online]. 2022 [visited on 2022-05-27]. Available from: <https://nano.ceitec.cz/nanofabrication-laboratory-equipment/>.
60. MICROCHEMICALS GMBH. *AZ® 1500-Series* [online]. 2022 [visited on 2022-05-27]. Available from: [https://www.microchemicals.com/products/photoresists/az\\_1518.html](https://www.microchemicals.com/products/photoresists/az_1518.html).
61. MICROCHEMICALS GMBH. *MIF Developers* [online]. 2022 [visited on 2022-05-27]. Available from: [https://www.microchemicals.com/products/developers/azr\\_726\\_mif\\_developer.html](https://www.microchemicals.com/products/developers/azr_726_mif_developer.html).
62. MICROCHEMICALS GMBH. *TechniEtch Cr01* [online]. 2022 [visited on 2022-05-27]. Available from: [https://www.microchemicals.com/products/etching\\_mixtures/technietch\\_cr01chromium\\_etchant.html](https://www.microchemicals.com/products/etching_mixtures/technietch_cr01chromium_etchant.html).
63. KLA CORPORATION [online]. 2022 [visited on 2022-05-27]. Available from: <https://www.kla.com/products/instruments/stylus-profilers/alphastep-d-600>.
64. *pySerial 3.4 documentation* [online]. 2020 [visited on 2022-06-04]. Available from: <https://pyserial.readthedocs.io/en/latest/>.